

A geometrically non-linear time-domain unsteady lifting-line theory

Hugh J. A. Bird *

Aerospace Sciences Division, School of Engineering, University of Glasgow, Glasgow, United Kingdom, G12 8QQ

Shūji Ōtomo †

School of Engineering, Institute for Energy Systems, University of Edinburgh, Edinburgh, United Kingdom, EH9 3BF

Kiran Ramesh‡

Aerospace Sciences Division, School of Engineering, University of Glasgow, Glasgow, United Kingdom, G12 8QQ

Ignazio Maria Viola§

School of Engineering, Institute for Energy Systems, University of Edinburgh, Edinburgh, United Kingdom, EH9 3BF

An unsteady lifting-line theory for time-domain problems with arbitrary kinematics is presented. This is formulated by matching a vortex particle based 2D inner model with a 3D vortex lattice wake. This and a small-amplitude frequency-domain unsteady lifting-line theory are then verified against experiment and computational fluid dynamics for the case of a flat rectangular plate oscillating in heave at aspect ratios 3 and 6. Both lifting-line theories were found to generally be in good agreement with experimental and CFD results, providing reasonable solutions even in cases dominated by LEV shedding. For larger amplitude problems, the new non-linear geometry lifting-line theory predicted larger amplitudes and higher average lift coefficient than the small-amplitude lifting-line theory.

Nomenclature

A_n	= Fourier coefficients
AR	= aspect ratio
c	= chord
s	= semispan
h	= plunge displacement
h_0	= plunge amplitude
$k = \omega c / 2U$	= chord reduced frequency
M	= a point on the wing surface
N	= number of inner solutions
t	= time
Δt	= time step
\mathbf{U}	= fluid velocity
v	= vortex core diameter
\mathbf{w}	= downwash
\mathbf{x}	= coordinate in global system
x, y, z	= coordinates
α	= angle of attack
Γ	= vorticity
γ	= vorticity density
θ	= angular coordinate on airfoil

*Graduate Researcher, h.bird.1@research.gla.ac.uk, Student Member AIAA

†Ph.D Student, School of Engineering, Institute for Energy Systems, s.otomo@ed.ac.uk

‡Lecturer, Aerospace Science Division, School of Engineering, Kiran.Ramesh@glasgow.ac.uk, Member AIAA

§Senior Lecturer, School of Engineering, Institute for Energy Systems, i.m.viola@ed.ac.uk

$\nu = \omega s/U$	=	span reduced frequency
ξ	=	Inner solution coordinate
ϕ	=	velocity potential

Subscripts

b	=	bound vorticity
d	=	drag
f	=	airfoil coordinate system
i	=	spanwise index
l	=	2D lift
L	=	3D lift
n	=	normal to airfoil
s	=	leading edge suction
∞	=	free stream

Abbreviations

LAULLT	=	large amplitude unsteady lifting-line theory
LLT	=	lifting-line theory
te	=	trailing edge
tev	=	trailing edge vortex
ULLT	=	unsteady lifting-line theory

Domains

I	=	inner domain
L	=	lifting-line
O	=	outer domain
S	=	wing surface
Σ	=	wake surface

Modifiers

\bullet'	=	coordinate in outer solution
\bullet	=	time derivative

I. Introduction

FOR the modern engineer, the leveraging of unsteady flow is becoming increasingly important in the pursuit of performance, efficiency and capability.

At the small scale, micro-air vehicle (MAV) designers are aiming to replicate the aerodynamic mechanisms employed by insects. MAVs typically operate at Reynolds numbers of $O(10^4)$ or less [1], making rotary wings an ineffective means by which to achieve hovering capability. It has been proposed that MAVs replicate the mechanism used by insects. Insects flap their wings to produce lift whilst hovering. Sufficient lift would not be generated were it not for the shedding of a free vortex from the leading edge of the insect's wing. This lift enhancing vortex is known as a leading edge vortex (LEV) [2].

At larger scales are energy harvesting mechanisms and flexible aerodynamic structures. Energy harvesting by vortex-induced motions can reduce the environmental impact and, potentially, the cost of renewable energy [3]. Mechanisms typically either depend upon shedding vortices from either side of a body, or upon generating vortices upstream of a body. These vortices induce forces that can be harvested for energy production.

Flexible aerodynamic structures can be found in high aspect ratio aircraft [4] and wind turbines [5]. The interaction of a flexible structure and its aerodynamics results in a computationally expensive coupled problem. Engineers must be able to verify that a control input or environmental perturbation will not lead to damaging loads on the structure [6], be able to model the outcome of control inputs and understand the implications of the mass and stiffness distribution across the structure during design [7].

All of the above involve the unsteady aerodynamics of wings. Such problems currently require expensive computational techniques such as computational fluid dynamics (CFD) [8–10] or the viscous vortex particle method (VVPM) [11, 12] to ensure that all physics are captured. This is a challenge during the design phase, where low cost simulation is required for optimization. And during use, these methods are too expensive for real-time simulation and control. This has lead to the development of low-order methods which aim to model only the most important physics of the problem. This is typically achieved within the framework of potential flow.

The common example is that of an airfoil in steady state. The airfoil is subject to lift. So long as the airfoil does not enter a stalled flow regime, viscosity can be neglected. For certain geometries the velocity potential field can be obtained using conformal mapping. This maps a cylinder containing vorticity in the complex plane to the real plane containing the problem geometry [13].

For more general geometries, the model can be further simplified by modelling the airfoil using thin airfoil theory [13]. Analytical or computational effort can be reduced due to the knowledge the thickness is much smaller than the chord of the airfoil. Boundary conditions can be moved the airfoil chord line. Such a model is only suitable for small angles of attack. It is therefore typically linearized.

Such gross simplifications can limit the applicability of a model such that its utility is lost. Selected important physical phenomena are therefore added to the simplified model. For example, the viscous boundary layer is added to a potential flow model in popular airfoil analysis packages such as XFOil [14] and JavaFoil [15].

For unsteady problems, quasi-steady thin airfoil theory can give inaccurate results [16]. This is because the wake, required to satisfy the Kelvin condition, is not present. The wake induces a downwash on the airfoil. Adding the unsteady wake to planar thin airfoils allowed the analysis of classic problems such as oscillating airfoils [17–19], impulsively starting plates [20] and the responses of airfoils to gusts [21, 22]. Arbitrary problems could be solved using the step functions models in conjunction with the Duhamel integral [23], and equivalence between frequency domain and time domain models can be shown [24]. Such models depend upon the satisfaction of the Kutta condition at the trailing edge to compute the strength of the wake, and assume that all amplitudes are small.

However, not all amplitudes are small. Extending unsteady models to large amplitudes requires non-linear geometry. Non-linear geometries typically require a numerical approach. These models can typically be divided into those that use the Milne-Thomson theorem [13] such as [25, 26], or models solved purely in the physical plane [27]. The latter are typically more flexible due the the former's requirement that geometry be transformed between the physical and complex planes.

Models that add only non-linear geometry cannot model dynamic stall [28]. Dynamic stall is the separation of the boundary layer occurring at the leading edge due to rapid changes in angle of attack. The newly formed shear layer then rolls up to form a leading edge vortex (LEV). The LEV, being in such close proximity to the airfoil, significantly affects the flow around the airfoil. This problem is typically tackled numerically. Darakananda and Eldredge place the models used into two groups [29]. Firstly, those that model the LEV as a single entity, being fed by the shear layer off the leading edge [29–31]. Secondly, those that model the shear layer using vortex elements and let it convect according to the laws of vortex dynamics [32–35]. The former model is simpler and better suited to real-time applications. The latter is slower, requiring the solution of the n-body problem, but can model a larger range of phenomena including large coherent vortex structures.

Many of these methods focus on a flat plate. The sharp leading edge leads to separation at the slightest perturbation, so it can be assumed that separation is always occurring. Such assumptions cannot be applied to the rounded leading edge of common airfoils however. Some form of shedding criterion is sought. Since boundary layer separation is strongly related to inverse pressure gradients on the surface of the airfoil, the leading edge suction of an airfoil [13] is a useful property by which separation might be determined, as in [32].

It is often the case that challenging phenomena such as LEVs affect the result of a model less than expected. McGowan et al. [16] showed that Theodorsen's theory [17] performed surprisingly well even when the assumptions of small amplitudes and trailing edge wake shedding were violated. This is because when an LEV is close to the surface of an airfoil, it acts as if part of the bound vorticity. Also, at higher frequencies of oscillation, the force required to accelerate the fluid around an airfoil - the non-circulatory force - can dominate the forces due the the airfoil's bound vorticity - the circulatory forces.

Extending two dimensional models to the third dimension has been challenging. Finite wings add additional phenomena to the problem. The most prevalent is Helmholtz's theorem: a vortex filament must not end in the fluid. In steady-state the basic requirement for lift is bound vorticity. A wing creating lift must therefore shed its bound vorticity into the wake. This wake induces a downwash on the wing. Matters are further complicated by the velocity induced on the wing by the wing itself.

The most simple method by which three dimensional problems can be modelled is to ignore these new phenomena. This leads to strip theory. Strips of the wing's span are modelled as independent two dimensional problems [23]. One of the primary advantages of this approach is the simplicity with which even a complex two dimensional solution can be applied a three dimensional problem.

If the wing's bound vorticity distribution varies sufficiently slowly in the span direction, the self-interaction of the wing surface with respect to span will be minimal. This is often the case for high aspect ratio wings. Neglecting this

self-interaction, but including the downwash induced by the wake leads to lifting-line theory (LLT).

In unsteady problems, complex wake structures can form even with low amplitude kinematics [36, 37]. A common problem is the oscillation of a plate. Unsteady lifting-line theories modelling this problem are numerous [38–42], but typically assume a planar wake with no self convection.

At larger amplitudes, dynamic stall again becomes an important phenomena. In its three dimensional guise, the LEV is more complex. Internal axial flow occurs along the length of a filament structure [43]. Even where the two dimensional problem does not appear to change with respect to span, internal axial flow can occur. This axial flow appears to play a role in the stabilization of LEV [44], making it an essential feature if insect wings are to be modelled. The LEV need not exist over the entire length of the wing. Commonly the LEV forms an arch structure terminating on the wing surface [10, 45]. The arch is highly three dimensional in nature, and causes strong three dimensional flows in its close vicinity.

Modelling the three dimensional flow around a wing has lead to the development of numerical methods. The most common of these is the unsteady vortex lattice method [13]. A vortex lattice represents both wing and wake. The wake is convected according to the laws of vortex dynamics. The numerical nature means that non-linear geometry and arbitrary kinematics can be modelled within easy to program and easy to extend framework. However, the large number of interactions within the method make it increasingly numerically expensive, and the inherent instability of a vortex sheet modelled by rings can cause practical difficulty.

More recently, and particularly in the domain of wind turbine analysis, methods that represent the free wake as a vortex particle sheet have become popular [46, 47]. These codes can be accelerated with tree-based algorithms [48, 49], although they remain computationally expensive. In three dimensions, vortex particle methods do not appear as robust as their two dimensional counterparts. The flow will eventually develop regions of high vorticity, or the particles may no longer represent the geometry of the vortex sheet. These problems can be tackled with redistribution and relaxation schemes [50]. Vortex particles can also be used to model viscous effects that are necessary for phenomena such as the merging of vortex particle rings.

Whilst such methods can be extended to include more complex phenomena such as LEV shedding [51], their numerical nature leads to a loss of emphasis on the phenomena of the problem.

The focus on phenomena makes unsteady lifting-line theories (ULLTs) attractive. In addition, by modelling only selected phenomena, the computational cost is reduced. The mathematical complexity of ULLTs has long remained a challenge however. A ULLT valid for all sized features in the wake [42] only exists in the frequency domain. This has been used to understand the validity of time domain ULLTs. Currently, even time domain methods assuming straight wings and small displacements [52, 53] are limited in terms of the frequency of their kinematics. Whilst a ULLT for non-linear geometry exists [54], being based on a 2D vortex element method [27], it too is frequency limited.

In terms of low-order modelling of wings, a laudable aim is perhaps a ULLT that is capable of modelling dynamic stall. The idea faces multiple hurdles. The biggest of these is due to the arch that a LEV structure often forms over the wing [10, 45]. The consequence of this is a rapid change of bound vorticity with respect to span, and, in the neighborhood of the arch structure, 3D flow. The requirement that vorticity change on the span scale, and that the flow over each chord section is approximately 2D is broken.

However, the foundations of lifting-line theory are often successfully used in violation of the assumptions on which lifting-line theory is based. Further challenges include the modelling of axial flow within the LEV. The simplicity of Drakananda and Eldredge's second, simpler set of 2D LEV shedding models lends themselves more easily to augmentation by axial flow within the LEV. The location and vorticity of the LEV core is known, allowing both change in 2D solutions with respect to span to be more easily computed and 3D induced effects to be more easily added. The reduction in computational expense would also be welcome.

The final two challenges of LEV shedding lifting-line models relate to the state of the art of small amplitude ULLTs. Firstly, the radius of the LEV is on the chord scale. Consequently, LEV shedding means the LEV must be capable of modelling chord scale wavelength features in its wake. Whilst in [42] this problem has been solved in the frequency domain, no solution has yet been obtained in the time domain.

Secondly, the LEV vortex core is unlikely to be straight. The repercussions of this are somewhat unclear. Guermond and Sellier [42] note that a ULLT is asymptotically invalid for a curved wing (with its consequently curved wake) for wake wavelength shorter than the span scale. This is because the wake induces velocities in the spanwise direction. Non-linear geometry leads to wake filament curvature due vortex roll-up. It may therefore be impossible to generate a geometrically non-linear time-domain ULLT valid for small wake wavelengths, let alone a theory that includes LEV shedding.

For all the mathematical obstacles that litter the path to an lifting-line theory that includes LEV shedding, low-order

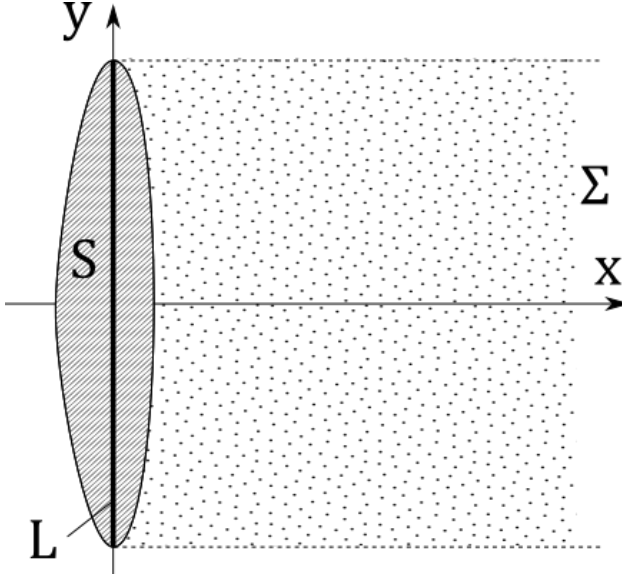


Fig. 1 A wing with surface S and its wake with surface Σ . The wing surface can be reduced to a lifting line L .

models can at times be accurate well beyond their limiting assumptions. A step in the direction of enriching ULLTs for more complex phenomena is therefore taken here. A numerical time-domain ULLT including non-linear geometry is formulated, valid for higher frequencies than the ULLT of Ramesh et al. [54]. As noted, the method may be valuable for problems with non-planar wakes and LEVs that effectively remain part of the bound vorticity. The large amplitude unsteady lifting-line theory (LAULLT) is formulated in section II, along with a description of a small amplitude LLT for comparison ([41]). An explanation of the experimental methods and CFD to be employed in this paper are given in section III and section IV respectively. The LAULLT and the small amplitude ULLT are then verified against CFD and experiment frequency domain problems in section V. Concluding remarks are given in section VI.

II. Theory

A high aspect ratio, straight wing is considered as shown in Fig. 1. The free stream acts in the x direction and the wing is free to move in pitch and heave. The wake is convected downstream in the x direction.

Since the wing is of high aspect ratio, AR, the semispan scale s is much larger than the chord scale c , so $AR = 2s/c \gg 1$. If we also assume that the bound vorticity, $\Gamma_b(y; t)$, varies on the span scale, we can apply lifting-line theory (LLT) to the problem.

The flow over a chord section of the wing is approximately two dimensional, with an extra induced velocity accounting for three dimensional finite wing effects. Since the wing is straight, these finite wing effects are due to the three dimensional wake. The extra induced velocity is the difference between the downwash induced by a two dimensional wake (already accounted for by the two dimensional problem) and a full three dimensional wake.

Close to a given chord section, the two dimensional problem's wake matches that of the three dimensional problem. The differences that lead to the extra induced velocity therefore only occur a distance on the span scale away from a given chord section. Working on the span scale means that the chord scale can be neglected and that the wing surface S contracts to a (lifting-) line, L . Hence, the downwash need only be computed on the lifting line. This span scale domain is called the outer solution, since s is the large variable. The small variable (c) solution is called the inner solution.

The inner solutions communicate their mutually induced velocities via the outer solution, with interaction occurring via the lifting line. Limiting the interaction reduces the number of variables to be solved simultaneously and allows the integration of two dimensional theories. For steady state, this was first done by Prandtl [55] although more complex schemes [56] are now used to integrate non-linear aerodynamics. The analytical treatment of unsteady problems is somewhat challenging. A solution for small amplitude harmonic oscillation of swept wings is given by Guermond and Sellier [42]. The implementation of Sclavounos' small-amplitude, harmonic oscillation ULLT [41] is far simpler, but it is limited to wake wavelengths larger than the chord scale, and straight wings.

In the time domain, pickings are far slimmer. Devinant [52] identified a framework for numerical unsteady

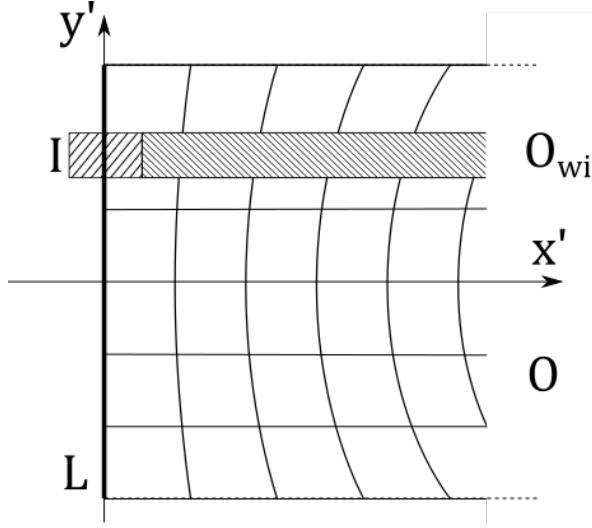


Fig. 2 A representation of the wing as a lifting line L and the consequent wake.

time-domain LLTs based upon the work of Guermond and Sellier [42]. This framework is used here.

For numerical consideration, the various sub-domains within the problem must be identified. Consider the wing surface S and its wake Σ as shown in Fig. 1. The wing can be represented by a straight lifting line L . This simplification is shown in Fig. 2, where the wake Σ has also been further subdivided into domains I , O_{wi} and O .

The domain I is the inner domain and is of radius c . This domain contains the bound vorticity about the wing section. The wake of the inner domain is convected downstream into the domain O_{wi} . Hence the inner problem considers the domain $I \cup O_{wi}$.

The outer problem is concerned with the outer wake. The domain containing the vorticity shed from the inner domain O_{wi} is also present in the outer domain. The wake of the lifting line not due to the inner domain I is the domain O . The entire wake of the lifting line is $O \cup O_{wi}$.

Consider the downwash $\mathbf{w}(M)$ at a point on the wing surface $M \in S$. It can be evaluated as the downwash from the inner 2D domain, plus some downwash due to finite wing effects from the outer domain:

$$\mathbf{w}(M) = \mathbf{w}_{in}(M) + \mathbf{w}_{out}(M) \quad (1)$$

where $\mathbf{w}_{in}(M)$ is the downwash from the inner domain and $\mathbf{w}_{out}(M)$ is the finite wing correction.

Due to lifting line approximation we can only evaluate the downwash due to the the domain $O \cup O_{wi}$ on the lifting line L . M on the lifting line is called M_0 . For frequency domain problems it has been shown by Ahmadi and Widnall [40] and Guermond and Sellier [42] that the complex downwash at any point M on S due to the outer domain can be computed from the complex downwash on the lifting line $\mathbf{w}_{out}(M_0)$:

$$\mathbf{w}_{out}(M) = \begin{Bmatrix} 0 \\ \mathbb{R}(e^{-ikx}\mathbf{w}_{out}(M_0)) \end{Bmatrix} \quad (2)$$

where $k = \omega c / 2U$ is the chord reduced frequency for a section oscillating at circular frequency ω .

However, a time-domain theory is sought, and the above cannot be applied. It become necessary to assume uniform downwash over the chord. The above allows an estimate of error to be found. Assuming uniform downwash over an inner solution is equivalent to setting $e^{-ikx} = 1$. Chord reduced frequency k must be of $o(1)$ for $e^{-ikx} \approx 1$. Since $AR \gg 1$ and $k = \nu/AR$, span reduced frequency ν must be at most of $O(1)$. The wake wavelength $\lambda = 2\pi U/\omega$ is of $O(s)/O(\nu)$. For validity, the wavelength is therefore $\lambda = O(s)$ or $\lambda \gg s$, or - for rectangular wings - $k \ll 1$.

To compute the downwash at any point on the lifting line, the contributions due to each part of the domain must be considered.

The velocity induced by the inner 2D domain $I \cup O_{wi}$ on $M \in I$ is given by

$$\mathbf{w}_{2D}(M) = \mathbf{w}_b(M) + \mathbf{w}_I(M) + \mathbf{w}_{wi}(M). \quad (3)$$

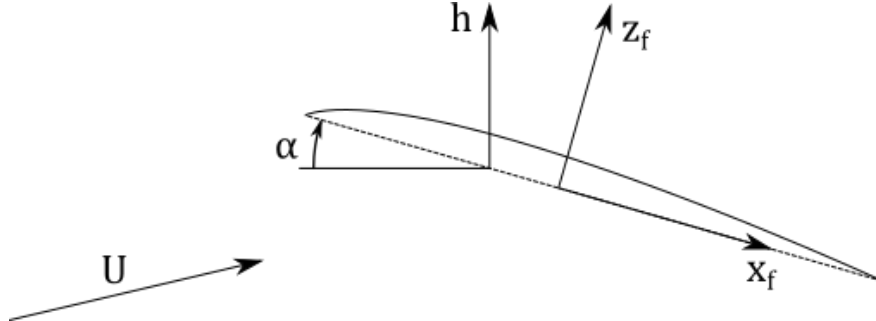


Fig. 3 Airfoil frame coordinate system for inner solution. The camber line of the airfoil is shown.

where \mathbf{w}_b indicates the effects of bound vorticity, \mathbf{w}_I the effect of vorticity in I and \mathbf{w}_{wi} the effect of shed vorticity in the inner domain that has been convected into O_{wi} . The downwash due to O_{wi} is accounted for in both the inner domain, and the outer domain $O \cup O_{wi}$. Hence it must be subtracted to obtain the first order complete downwash:

$$\mathbf{w}(M) = \mathbf{w}_{2D}(M) + \mathbf{w}_{out}(M_0) - \mathbf{w}_{wi}(M_0) + o(1/A) \quad (4)$$

Additional terms are needed if a swept or curved wing is to be considered.

A. Inner solution

The inner solution is modeled on the large amplitude unsteady thin airfoil theory of Ramesh et al. [27], although any vortex shedding theory could be substituted (for example Yan et al. [26], Katz and Plotkin [13], or McCune et al. [25]). Interested readers should refer to [27] for further details.

The i th inner solution on the lifting line is at $y = y_i$ on L where $i = 0, 1, \dots, N$ and $y_i < y_{i+1}$. It can be considered as if almost in isolation. The interaction between inner solution is via the wake and the induced downwash. Due to the induced downwash, the local free stream, \mathbf{U} , from the perspective of the inner solution, is

$$\mathbf{U}(y_i; t) = \mathbf{U}_\infty + \mathbf{w}_{out}(M_0(y_i)) - \mathbf{w}_{wi}(M_0(y_i)) \quad (5)$$

where \mathbf{U}_∞ is the free stream velocity.

The inner solution uses a two dimensional coordinate system. A point in this system is denoted by ξ .

The airfoil frame coordinate system used is shown in Fig. 3, where the chord is on $x_f \in [-c/2, c/2]$, where $x_f = -c/2$ is the leading edge. The bound vorticity distribution over the foil can be modeled using a Fourier series with an additional leading edge singularity,

$$\gamma_b(y_i; t) = 2|\mathbf{U}_\infty| \left(A_0(y_i; t) \frac{1 + \cos(\theta)}{\sin(\theta)} + \sum_{n=1} \bar{A}_n(y_i; t) \sin(n\theta) \right) \quad (6)$$

where γ_b is the bound vorticity density on the airfoil, $x_f = \frac{c}{2} \cos(\theta)$ and A_n are unknown coefficients. In steady state, this satisfies the Kutta condition implicitly. The deviation from the Kutta condition in unsteady problems seems to have little by way of consequences. This expression can be integrated to find the total bound vorticity, Γ_b associated with the chord section

$$\Gamma_b(y_i; t) = \frac{|\mathbf{U}_\infty| c(y_i)}{2} \pi \left(A_0 + \frac{A_1}{2} \right) \quad (7)$$

The coefficients A_n can be found by applying a Neumann boundary condition on the airfoil. Consequently they are calculated as

$$A_0(y_i; t) = -\frac{1}{\pi} \int_0^\pi \frac{W}{|\mathbf{U}_\infty|} d\theta \quad (8)$$

$$A_n(y_i; t) = \frac{2}{\pi} \int_0^\pi \frac{W}{|\mathbf{U}_\infty|} \cos(n\theta) d\theta \quad (9)$$

where W is the downwash on the airfoil section at y_i . The downwash includes components from the free stream, any downwash induced by movement, and the induced velocity of the wake.

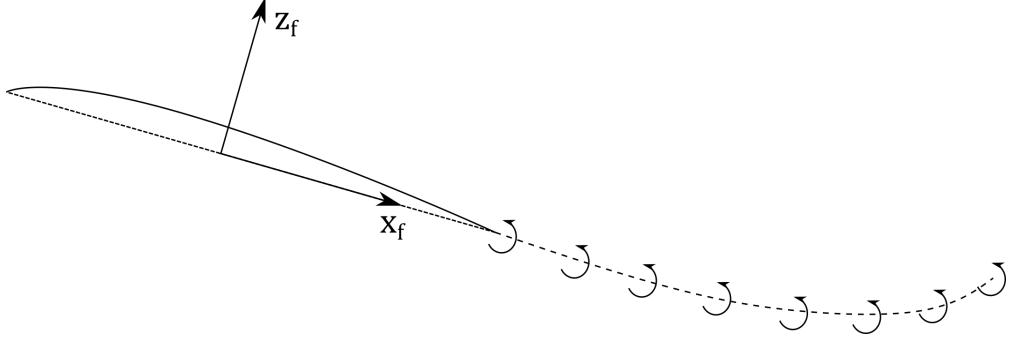


Fig. 4 Wake shedding from the trailing edge of the inner solution. The camber line of the airfoil is shown.

The wake sheet is represented by regularized vortex particles. A time marching procedure is used to generate new particles. The m th particle has radius ν , position $\xi_{i,m}$ and vorticity $\Gamma_{i,m}$. Using the Vatistas, Kozel & Mih [57] regularization, the induced velocity induced by the m th vortex particle at a point ξ can be computed.

$$\frac{\partial \phi_{i,m}}{\partial \xi_1} = \frac{\Gamma_{i,m}}{2\pi} \frac{\xi_2 - \xi_{i,m_2}}{\sqrt{((\xi_1 - \xi_{i,m_1})^2 + (\xi_2 - \xi_{i,m_2})^2)^2 + \nu^4}} \quad (10)$$

$$\frac{\partial \phi_{i,m}}{\partial \xi_2} = -\frac{\Gamma_{i,m}}{2\pi} \frac{\xi_1 - \xi_{i,m_1}}{\sqrt{((\xi_1 - \xi_{i,m_1})^2 + (\xi_2 - \xi_{i,m_2})^2)^2 + \nu^4}} \quad (11)$$

where $\phi_{i,m}$ is the velocity potential field of the m th particle.

This allows the downwash W to be calculated:

$$W(x_f, y_i; t) = \frac{\partial \eta}{\partial x_f} \left(\mathbf{U} \cdot \begin{Bmatrix} \cos \alpha \\ -\sin \alpha \end{Bmatrix} + \dot{h} \sin \alpha + \frac{\partial \phi_{tev}}{\partial x_f} \right) - \mathbf{U} \cdot \begin{Bmatrix} \sin \alpha \\ \cos \alpha \end{Bmatrix} - \frac{\dot{a}c}{2} (x_f - a) + \dot{h} \cos \alpha - \frac{\partial \phi_{tev}}{\partial z_f} \quad (12)$$

where ϕ_{tev} is the sum of the trailing edge vortex velocity potentials, α is the angle of attack, h is the plunge displacement and \bullet indicates the derivative in time. η represents the camber distribution of the airfoil.

The time marching technique requires new vortex particles to be shed into the wake of the airfoil. A vortex particle shed at time-step m (and $t = t_m$) is placed at

$$\xi_m|_{t_m} = \begin{cases} \xi_{te}|_{t_m} + \frac{2\Delta t}{3}(\mathbf{U} + \dot{\xi}_{te}|_{t_m}), & \text{if } m = 0 \\ \xi_{te}|_{t_m} + \frac{2}{3}(\xi_{m-1}|_{t_m} - \xi_{te}|_{t_m}), & \text{otherwise} \end{cases} \quad (13)$$

where ξ_{te} is the coordinate of the trailing edge. The vortex core radius is approximately 1.3 times the spacing between the particles.

To compute the strength of a new vortex particle the Kelvin condition is needed.

$$\Gamma_b(t_m) + \sum_{p=0}^m \Gamma_p = 0 \quad (14)$$

The strength of the new particle solved linearly by computing the effect of the new vortex particle on coefficients A_0 and A_1 .

The normal force on the airfoil can be computed as

$$C_n(y_i; t) = \frac{2}{|\mathbf{U}_\infty|} \left[\left(\mathbf{U} \cdot \begin{Bmatrix} \cos \alpha \\ -\sin \alpha \end{Bmatrix} + \dot{h} \sin \alpha \right) \left(A_0 + \frac{1}{2} A_1 \right) + c \left(\frac{3}{4} \dot{A}_0 + \frac{1}{4} \dot{A}_1 + \frac{1}{8} \dot{A}_2 \right) \right] + \frac{2}{c |\mathbf{U}_\infty|^2} \int_{-c/2}^{c/2} dx_f \frac{\partial \phi_{tev}}{\partial x_f} \gamma_b(x_f, t) \quad (15)$$

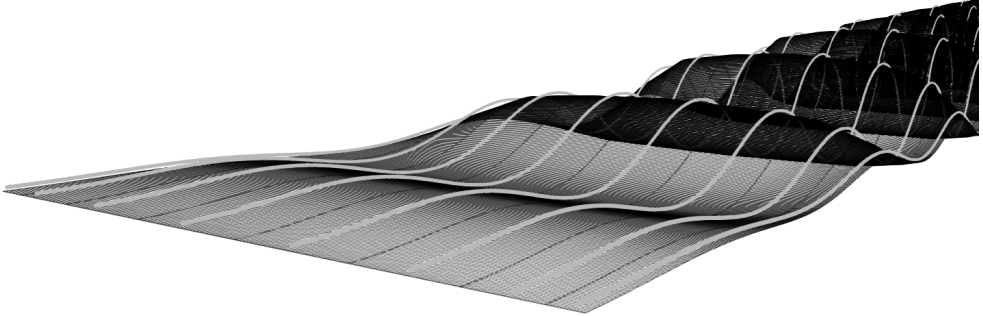


Fig. 5 Interpolation of the vortex particles to form a vortex lattice in the outer domain.

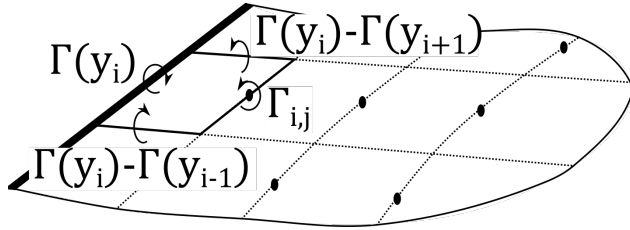


Fig. 6 Assembly of the vortex lattice.

And the leading edge suction force is

$$C_s(y_i; t) = 2A_0^2 \quad (16)$$

From C_n and C_s the lift and drag coefficients can be found.

$$C_l(y_i; t) = C_n \cos \alpha + C_s \sin \alpha \quad (17)$$

$$C_d(y_i; t) = C_n \sin \alpha - C_s \cos \alpha \quad (18)$$

B. The outer wake

The wakes of the inner solutions must be interpolated to produce the wake in the outer solution. The first step in this process is the transformation of a point in an inner solution in \mathbb{R}^2 to a point in the outer solution in \mathbb{R}^3 . In the outer solution the lifting line is assumed to be straight, hence the displacement from the trailing edge is used.

In the outer solution, a point $\mathbf{x}' = \{x', y', z'\}$ on the wake is assumed to be shed from the lifting line L which lies on $x' = z' = 0 \in y' = [-s, s]$. Hence for a point ξ in an inner solution that lies at $y = y' = y_i$,

$$\mathbf{x}' = \begin{Bmatrix} \xi_1 - \xi t \mathbf{e}_1 \\ y_i \\ \xi_2 - \xi t \mathbf{e}_2 \end{Bmatrix} \quad (19)$$

Now that points have been transferred to the outer domain, they can be interpolated. At $t = t_m$ the m th vortex particle was shed in each inner solution. These can be interpolated across the $i = 0, 1, \dots, N$ inner solutions. Cubic spline interpolation is used [58]. Where $y < y_0$ or $y > y_N$ the cubic spline is linearly extrapolated.

Using the interpolation of the vortex particles, a vortex lattice can be assembled. Figure 5 shows an assembled lattice along with its parent vortex particles. Practicality demands that straight vortex filaments are used. The splines are evaluated at $y = \{-s, (y_0 + y_1)/2, (y_1 - y_2)/2, \dots, (y_{N-1} + y_N)/2, s\}$ to create an $N + 2$ by m grid of points. The grid is extended by 1 in the m direction such that it is $N + 2$ by $m + 1$ by interpolating the lifting-line at the y locations. From this a lattice can be constructed. Filaments representing the vorticity of vortex particles are placed such that they pass through a vortex particle in the N direction on the grid. The vorticity of these filaments is set to match the vorticity of the particle they pass through. Filaments on the lifting line match the bound vorticity of the wing. In the m direction the strength of filaments are set according to Helmholtz's theorem. Consequently, they represent the history of the $\partial\Gamma_b/\partial y$. These can be seen in Figure 6.

We can evaluate the induced velocity on a point due to this vortex lattice using the Biot-Savart law for straight filaments [13]. Evaluating this on the lifting-line gives $\mathbf{w}_{out}(M_0)$ for the i th inner solution if we evaluate the downwash at the point $M_0 = \{0, y_i, 0\}$. During this calculation the vortex filaments that make up the lifting-line can be ignored.

We also want to compute $\mathbf{w}_{wi}(M_0)$. This is computed much like in 2D, except that coordinates from the outer system are used. On a strip i

$$\mathbf{w}_{wi}(y_i) = \begin{cases} \sum_{p=0}^m \frac{-\Gamma_{i,p}}{2\pi} \frac{z'_{i,p}}{x_{i,p}^2 + z_{i,p}^2} \\ 0 \\ \sum_{p=0}^m \frac{\Gamma_{i,p}}{2\pi} \frac{x'_{i,p}}{x_{i,p}^2 + z_{i,p}^2} \end{cases} \quad (20)$$

The vortex particle are constrained to their inner solutions planes at $y = y_i$. Additionally the downwash from the three dimensional wake is only computed on the lifting-line. As a consequence wake roll-up cannot occur in the outer wake. This does not stop wake roll-up from occurring in the inner wake.

To compute the coefficients, the local coefficients are summed.

$$C_L(t) = \frac{1}{A} \sum_{i=0}^N C_l(y_i; t) c(y_i) \delta_i \quad (21)$$

$$C_D(t) = \frac{1}{A} \sum_{i=0}^N C_d(y_i; t) c(y_i) \delta_i \quad (22)$$

where δ_i is the length of span represented by the i th inner solution and A is the wing area. Remaining consistent with the earlier discretization,

$$\delta_i = \begin{cases} \frac{y_{i+1} - y_{i-1}}{2}, & \text{if } 0 < i < N \\ \frac{y_1 + y_0}{2} + s, & \text{if } i = 0 \\ s - \frac{y_{N-1} + y_N}{2}, & \text{if } i = N \end{cases}$$

C. Algorithm

The time marching algorithm is as follows:

- 1) Construct the outer solution.
- 2) Compute velocities induced by outer solution.
- 3) Place new vortex particle in each inner solution.
- 4) Solve the inner solution.
- 5) Convect vortex particles in inner solution.

It is notable that the inner solutions can solve for the strength of new vortex particles independently of other inner solutions. This can be justified by the fact that the new vortex particle remains in very close proximity to the chord section, in domain I . The detail of the new vortex particle need not be communicated for the same reason that the detail of the bound vorticity need not be communicated - it is on L .

The method scales well in comparison to vortex lattice or vortex particle methods. The n-body calculation required for convection dominates the computational cost. For this LAULLT, the computational cost is of $O(Nm^2)$. This contrasts with the cost of the vortex lattice method, which costs $O(N^2m^2)$. A vortex particle method would require more evaluations since a great number of particles would be required across the span.

A secondary benefit is the robustness of the method. Maintaining the stability of a UVLM or vortex particle method over long time periods can be challenging. Whilst the instability of vortex sheets eventually leads to a somewhat disordered far wake in the inner solution, this does not affect the stability of the LAULLT solution as a whole.

D. Limitations

The formulation of LAULLT limits the validity of the method. ULLTs assume that aspect ratio is large. On the span scale, the wing is assumed to be straight. Variation in the chord should occur on the span scale. Additionally, variation in bound vorticity should also occur on the span scale. As with all lifting-line theories, this technically limits the theory to wings with cusped tips, but in practice it can be applied to wings with square tips successfully. Whilst the downwash induced on the lifting-line is not limited with respect to frequency, the assumption that the wash in the inner solution is uniform limits the method to wake wavelengths of the span scale or larger. This limits the otherwise arbitrary kinematic input. Finally, the method is subject to the restrictions of the inner solution. In this case, invicid, incompressible and irrotational flow with no LEV shedding.

E. Sclavounos' unsteady lifting line theory

The LAULLT will be compared to a small-amplitude harmonic-oscillation ULLT.

Sclavounos' method [41] is valid for straight wings and wake wavelengths of the chord scale or larger. This corresponds to a chord reduced frequency $k < 1$. Like the LAULLT, uniform downwash is assumed in the inner solution. Details on the implementation of the method can be found in [41, 59].

III. Experimental methods

Direct force measurements and particle image velocimetry are performed in the water flume at the University of Edinburgh. The water flume is 400 mm wide, the water depth is 340 mm and free stream velocity ranges up to 1 m/s.

A flat plate with a blunt leading edge, made of aluminum with $c = 100$ mm, $2s = 300$ mm, and 2 mm thickness is submerged in an inflow speed of 0.1 m/s, resulting in the chord based Reynolds number of 10000. The plunging foil rig consists of two linear motors (LinMot, PS01-23x80F-HP-R20) connected with each other via a linkage system and a coupler plate (see Figure 7). A six-axis force/torque sensor (ATI Inc., Nano-17 IP68) is mounted between the coupler plate and the foot plate. The Nano17 sensor can measure forces in the plane of the wing cross section up to ± 25 N, and ± 35 N in the orthogonal direction, and moments up to ± 250 Nmm around the three axes, with a resolution of 1/160 N for the forces and 1/32 Nmm for the moments. LabVIEW is used to trigger the prescribed motor motion through a digital output device and also to start recording forces for a synchronised measurement through a DAQ board. Forces of 8 periods are recorded at a sampling frequency of 10 kHz. The recorded force data are low-pass filtered by the forth-order Butterworth filter with the cutoff frequency of 16 times the plunging frequency, following which phase-averaging is applied for 6 periods without the first and the last period of force data.

Flowfield analysis is performed using particle image velocimetry (PIV). A double pulsed Nd:YAG laser (New Wave Research, Solo PIV, 532 nm, 200 mJ) is used to illuminate the plane at 1/4 of the span of the wing ($y = 0.5s$). Silver coated hollow glass spheres (Dantec Dynamics, 10 μm) are used as seeding. Images are obtained by a CCD camera (IMPERX, B2020 equipped with Nikon 50 mm lens) with a resolution of 2056 pix \times 2060 pix. Adaptive multi-pass cross-correlation is employed to compute velocity vectors, with a first interrogation window of 64 pix \times 64 pix, and a second interrogation window of 32 pix \times 32 pix, and an overlap of 50% (DaVis, LaVision Inc.). 4 periods of PIV data are used for phase-averaging.

IV. Computational Fluid Dynamics

High-fidelity 3D computations of unsteady fluid dynamics are performed at Reynolds number of 10,000 using the open-source CFD toolbox OpenFOAM. A body-fitted computational mesh is moved in accordance with prescribed rate laws, and the time-dependent incompressible Navier-Stokes are solved using a finite-volume method. A second-order backward implicit scheme is adopted to discretize the transient terms, while second-order, limited Gaussian integration schemes are used for the gradient, divergence and Laplacian terms. The pressure implicit with splitting of operators (PISO) algorithm is employed to achieve pressure-velocity coupling. The Spalart-Allmaras (SA) turbulence model [60] is used for turbulence closure. The SA model is chosen for this problem because of extensive previous experience in applying it successfully for unsteady, separated and vortex-dominated flows at $Re = 10,000$ such as those considered in

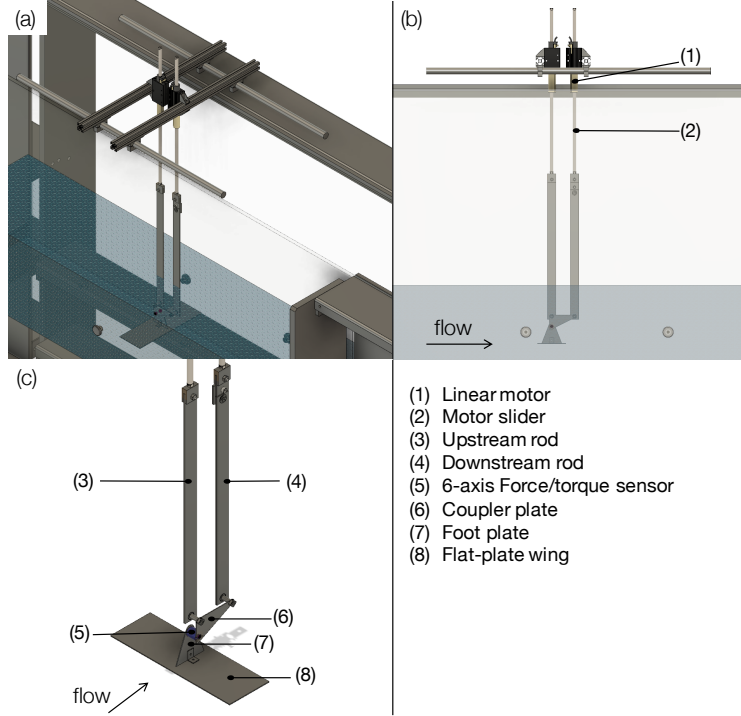


Fig. 7 Test section and experimental setup: (a) in the flume, (b) side view, (c) detailed view

this research [16, 32]. The trip terms in the original SA model are turned off, and for the low Reynolds number cases considered in this research, the effects of the turbulence model are confined to the shed vortical structures and wake.

The airfoil chord length $c = 0.1\text{m}$. An O-mesh is constructed, which has 164 cells chordwise, with increased resolution near the leading and trailing edges. The average spanwise spacing on the wing is $c/72$, with increased resolution at the wingtip. The spanwise domain extends 2 chord lengths beyond the wingtip with an average spacing of $c/40$ in this region. In the wall-normal direction, cell spacing begins at $4 \times 10^{-5} \text{ m}$ next to the wall ($y+ < 1$) and is constrained to maximum spacing of $c/100$ up to a distance of $1.3c$ away from the wing, and has a maximum spacing of $c/20$ up to a distance of $6c$ from the wing in order to resolve the trailing wake. From thereon, a coarser mesh extends to $12c$ from the wing with a maximum spacing of $c/5$. The simulations were carried out at a free stream velocity $U = 0.1 \text{ m/s}$ and kinematic viscosity $10^{-6} \text{ m}^2/\text{s}$.

V. Results and discussion

Results are compared for a flat rectangular plate oscillating in heave at a constant angle of attack. Lift coefficient, C_L , from the LAULLT and Sclavounos's ULLT are validated against CFD and experiment for the aspect ratio 3 plate, and against CFD for the aspect ratio 6 plate. The CFD and experiment are also compared to each other.

The plate oscillates in heave, such that the z displacement of the plate is defined by $h_0 \sin(\omega t)$. The motion is defined in terms of chord reduced frequency $k = \omega c / 2U_\infty$ and normalized heave amplitude h_0/c . Four cases were considered, as detailed in Table 1.

For all the cases the LAULLT wing was discretized into 16 strips of equal width. This produced a result within 1%. Data was taken after approximately 50 chord lengths had been travelled. This was the 6th oscillation for $k = 0.4$ and from the 16th oscillation for $k = 1$. By this point the result had converged within 1% of the final solution. For the inner solution, eight Fourier terms were used at $U\Delta t/c = 0.015$ as was used in [32].

Sclavounos' ULLT results were computed using 8 Fourier terms to approximate the bound vorticity distribution. Sclavounos' ULLT [41] only computes the unsteady part of the solution. As a linear theory it can be summed with a steady-state solution. This was obtained using Prandtl's LLT [55] using 16 Fourier terms to approximate the steady-state bound vorticity distribution. The LAULLT naturally includes steady lift components and needs no such augmentation.

Tabulated numerical results are available in the appendix. These give the amplitude of the lift coefficient, C_L ,

Table 1 Case kinematics. For all cases the angle of attack is constant at $\alpha = 4$ degrees and the experimental Reynolds number $Re = 10,000$.

Case	k	h_0/c
1	0.4	0.05
2	0.4	0.5
3	1.0	0.05
4	1.0	0.5

defined by the peak to peak amplitude divided by two and the average value of C_L .

A. Case 1: $k = 0.4, h_0/c = 0.05$

Harmonic plunging oscillations with $k = 0.4$ and $h_0/c = 0.05$ are considered in this case. The amplitude is small, so the planar wake assumption, and hence Sclavounos' ULLT, is expected to give good results.

Figure 8 shows a comparison between the vorticity field of the PIV and CFD data at the quarter-span of the wing. There is a good agreement between the methods. The boundary layer is thicker on top surface of the wing at the leading edge due to the small angle of attack. No LEVs form during the oscillation, although the boundary layer does separate at the leading edge.

Figure 9a shows a comparison of the C_L curves for the AR3 case. Both experiment and CFD predict different average C_L s to the potential flow based theories indicating aerodynamic non-linearity. The sharp leading edge leads the boundary layer to separate at the leading edge and reattach further down stream, creating a bubble. This viscous phenomena cannot be accounted for in either the Sclavounos / Prandtl model or the LAULLT due to the invicid assumption. Such bubbles typically result in increased lift.

The LAULLT and Sclavounos / Prandtl ULLT solutions are in good agreement. The C_L amplitudes predicted by the methods are also in good agreement with the predictions of the CFD and experiment. There is a small phase difference between the lift predicted by the LAULLT and the Sclavounos ULLT, and the CFD and experimental solutions.

At aspect ratio 6, shown in Figure 9b, the LAULLT and Sclavounos / Prandtl solutions are again in good agreement. Both once again predict a smaller C_L amplitude and average than the CFD. There is also a small phase error.

B. Case 2: $k = 0.4, h_0/c = 0.5$

The chord reduced frequency is maintained at $k = 0.4$ whilst the amplitude is increased by a factor of 10 to $h_0/c = 0.5$.

This leads to an increasingly non-planar wake and to LEV shedding. This is shown in Figure 10, with the good agreement between the CFD and PIV results shown in Figure 11. The tip vortex forms on the entirety of the wing tip, not just at the trailing edge. The wake of the wing tip lies close to the path of the tip through the fluid - compared to the more central sections of the wing, wake deformation is relatively minimal.

At the quarter span, $y = 0.5s$, LEV shedding and geometric non-linearity is evident. This is shown in both Figure 10 and Figure 11. On the upwards stroke ($-0.25 < t/T < 0.25$) the boundary layer substantially thickens on the underside of the leading edge but does not separate to form an LEV. On the downwards stroke ($0.25 < t/T < 0.75$) an LEV is formed on the upper surface of the airfoil. The LEV travels along the upper surface of the airfoil before becoming part of the trailing edge wake. This trailing edge wake is non-planar both due to the large displacements and the deformation caused by the significant vorticity within it.

At the wing root stronger vortices are formed than at the tip. On the upwards stroke the boundary layer separates from the airfoil. On the downwards stroke the LEV becomes sufficiently large as to separate from the surface of the airfoil.

The C_L history is shown for both aspect ratios in Figure 12. The non-sinusoidal shape of the experimental and CFD results is noticeable. The asymmetric shape is due to the asymmetric formation of LEVs. The distortion is most noticeable for $0.5 < t/T < 1.0$, during the latter stages of the growth and then separation of the LEV during the downwards stroke. This asymmetric LEV shedding is caused by the small angle of attack of the airfoil.

Figure 12b shows the C_L history for the aspect ratio 6 case. The deformation of the waveform due to this LEV

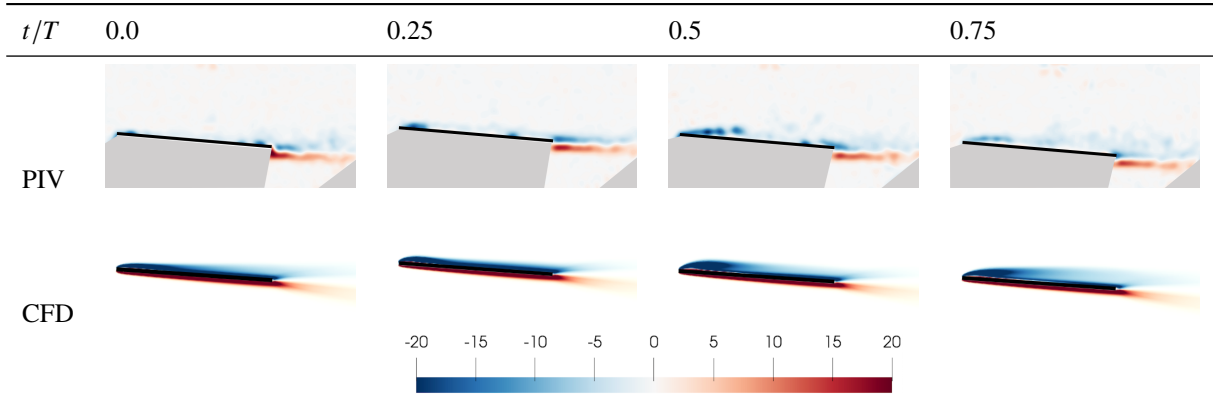


Fig. 8 Normalized spanwise vorticity $\omega_y c/U$ comparison between experimental PIV data and CFD for case 1: $k = 0.4$, $h_0/c = 0.05$, $\text{AR} = 3$ and $y = 0.5s$.

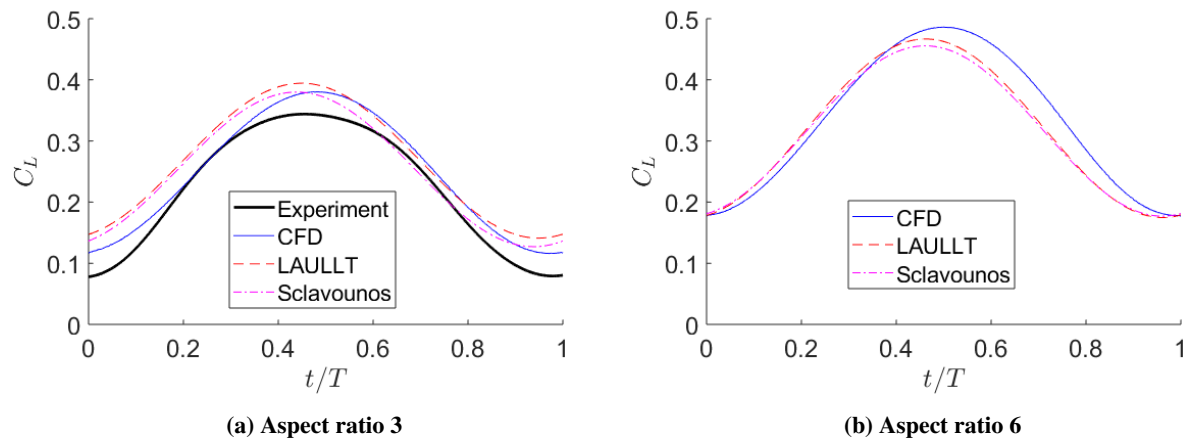


Fig. 9 C_L history for case 1: $k = 0.4$, $h_0/c = 0.05$

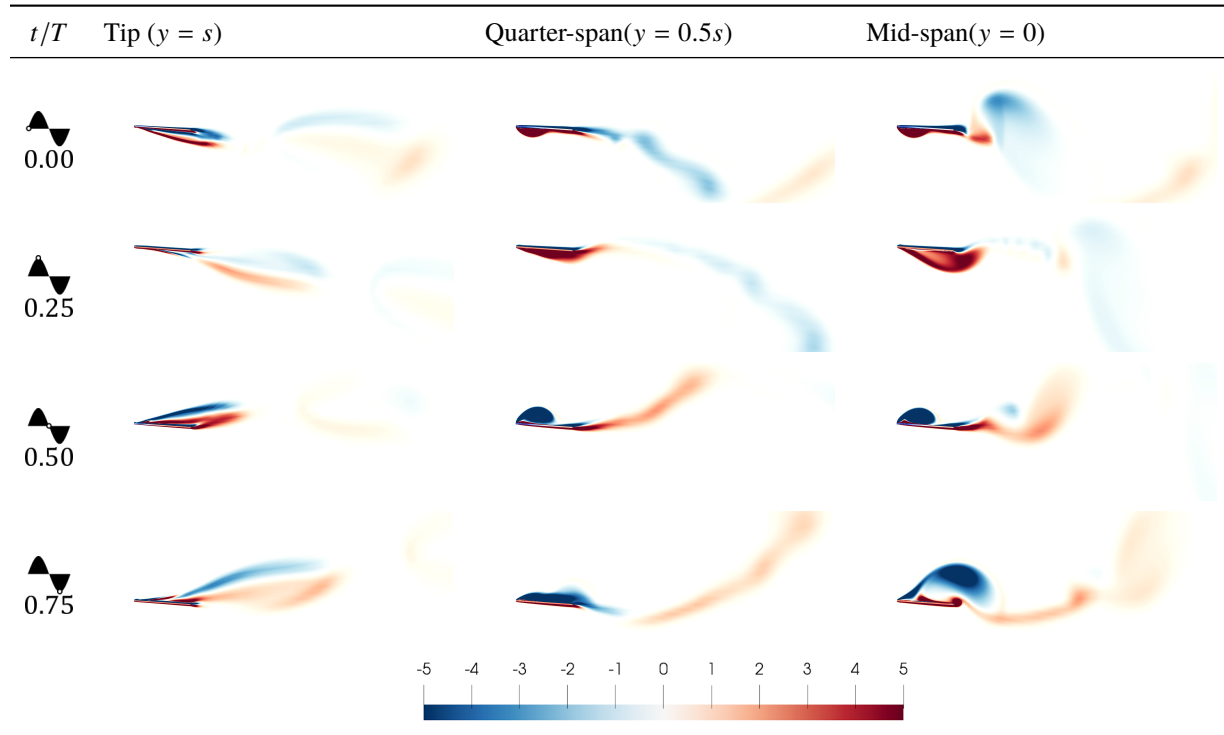


Fig. 10 Normalized spanwise vorticity $\omega_y c/U$ from CFD for case 2: $k = 0.4$, $h_0/c = 0.5$, $\text{AR} = 3$.

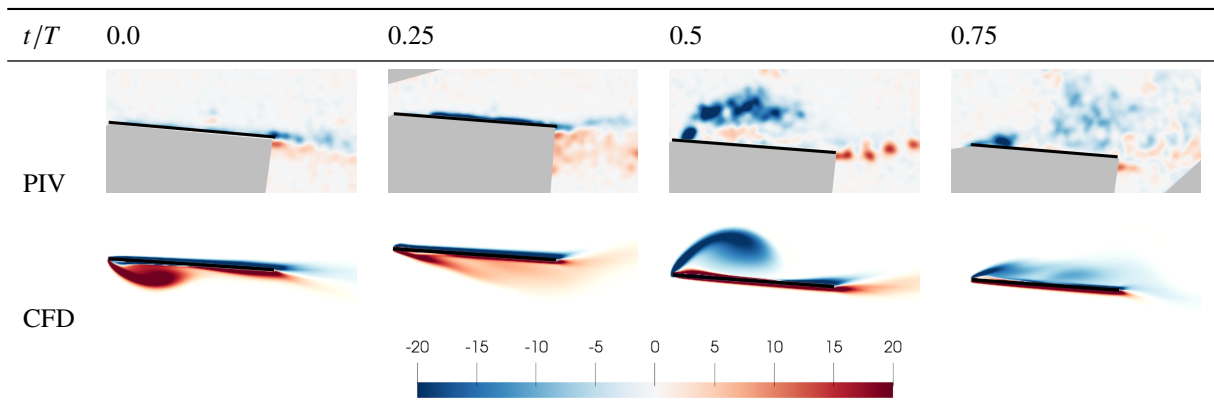


Fig. 11 Normalized spanwise vorticity $\omega_y c/U$ comparison between experimental PIV data and CFD for case 2: $k = 0.4$, $h_0/c = 0.5$, $\text{AR} = 3$ and $y = 0.5s$.

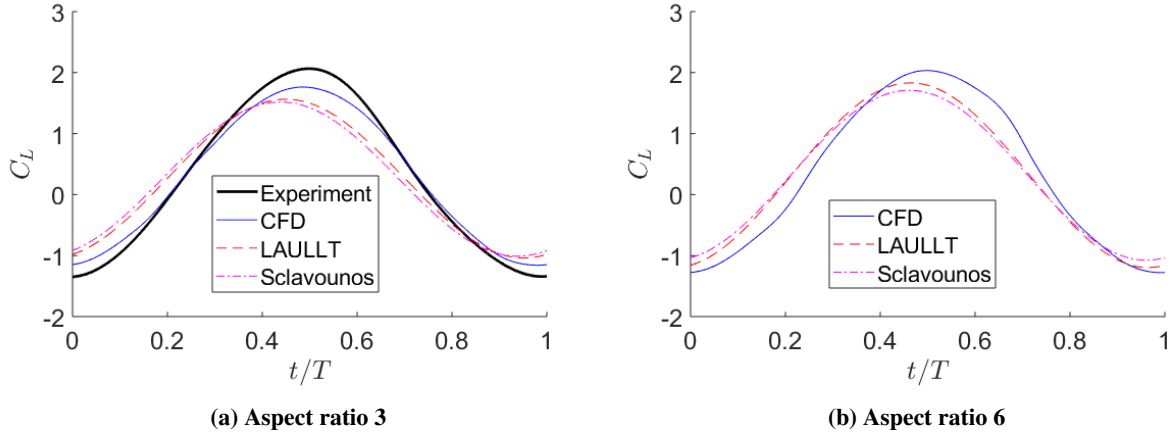


Fig. 12 C_L history for case 2: $k = 0.4$, $h_0/c = 0.5$

shedding is increased at higher aspect ratio, since LEV shedding occurs over a greater portion of the wing's span. Since the ULLTs do not model LEVs, the waveforms produced are sinusoidal in shape.

The experiment and CFD match well in phase, but the experimental solution exhibits a larger lift amplitude. Both the LAULLT and Sclavounos / Prandtl solutions are in close agreement. They predict a smaller C_L amplitude than either the experimental or CFD solutions. Again, the results show a small phase difference.

In comparison to case 1 ($k = 0.4$, $h_0/c = 0.05$), the C_L amplitude scaled linearly with oscillation amplitude for Sclavounos' ULLT. The average C_L remained the same. The effects of the planar wake assumption of Sclavounos' method therefore appear to be negligible. Comparatively, the experimental and CFD C_L amplitudes have grew by more than a factor of 10. The CFD and experiment featured LEVs at $h_0/c = 0.5$ not present at $h_0/c = 0.05$.

At aspect ratio 6, the phenomena remain similar. Consequently the analysis of flow phenomena remains similar. The difference between the result obtained using CFD and the results of the ULLTs become larger, although the LAULLT and Sclavounos / Prandtl solutions are again in very good agreement. The lifting-line theories again do not reproduce the non-sinusoidal shape produced by the CFD, and the phase error remains.

C. Case 3: $k = 1$, $h_0/c = 0.05$

The frequency is increased to $k = 1$ and the amplitude is returned to the amplitude of $h_0/c = 0.05$. Spanwise vorticity plots of the CFD are shown in Figure 13. A comparison of CFD and PIV at the quarter span, $y = 0.5s$, is shown in Figure 14.

At the wing tip, the wake remains planar. Moving towards the middle of the wing, the vorticity field at the quarter span and the centre of the wing are very similar. In both cases a small LEV forms at the leading edge on the upper side of the airfoil on the downwards stroke ($0.25 < t/T < 0.75$). This LEV remains attached and travels along the upper surface of the airfoil as seen at $t/T = 0.0$. The earlier stages of this are more visible in the comparison between the CFD and PIV in Figure 14, but differences in scale make the later stages more visible in Figure 13. The boundary layer on the bottom of the airfoil remains thin. Figure 14 shows that the CFD and PIV data are in good agreement.

Figure 15a shows the lift histories for the aspect ratio 3 case. The waveforms produced by the CFD and experiment differ at the peaks, with the experimental peaks being sharper. The CFD waveform is more sinusoidal. The phase of the CFD and experiment are in reasonable agreement.

The ULLTs are in very close agreement. They match the amplitude of the experimental results but do not reproduce its non-sinusoidal shape. In comparison to the CFD, the predicted C_L amplitude is much larger. There is a phase difference between the results of the ULLTs and the experiment and CFD.

Aspect ratio 6 results are shown in Figure 15b. The agreement of the ULLTs is slightly worse than at aspect ratio 3, but still close. The LAULLT predicts a slightly larger C_L amplitude. Both ULLTs give a sinusoidal waveform similar to that of the CFD result. However, the C_L amplitude is larger than that of the CFD and there is a small phase error.

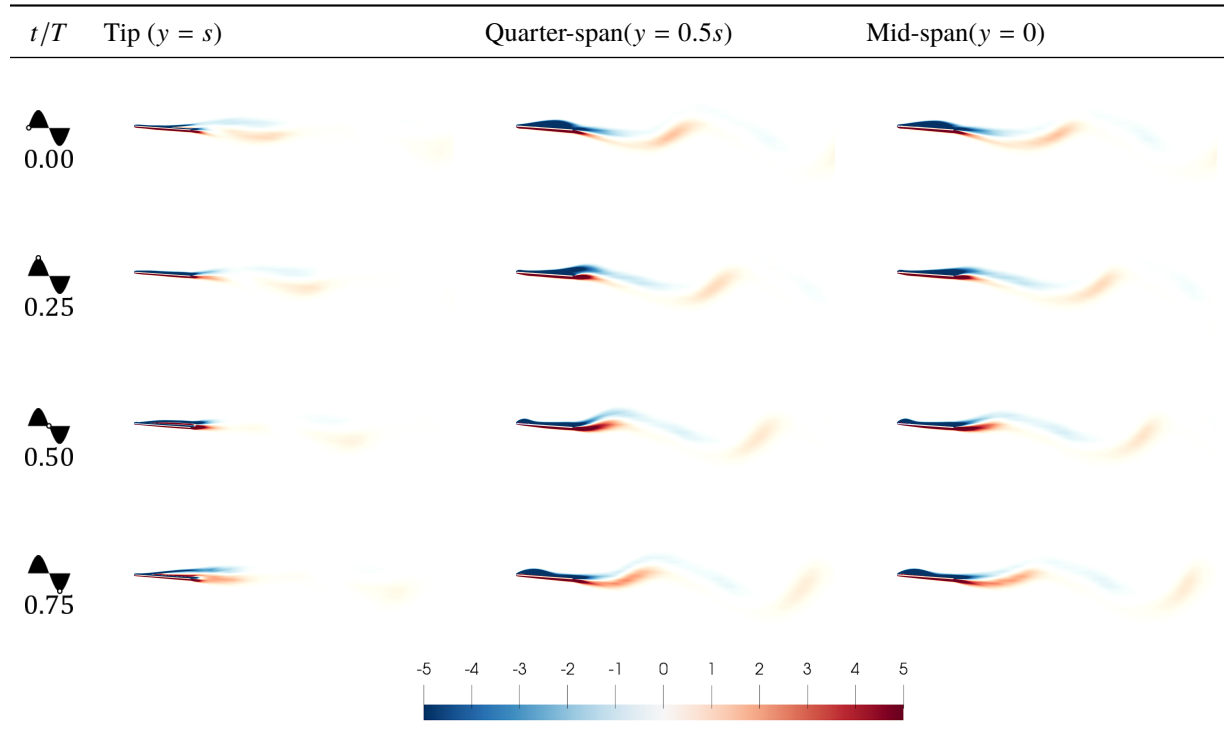


Fig. 13 Normalized spanwise vorticity $\omega_y c/U$ from CFD for case 3: $k = 1$, $h_0/c = 0.05$, $\text{AR} = 3$.

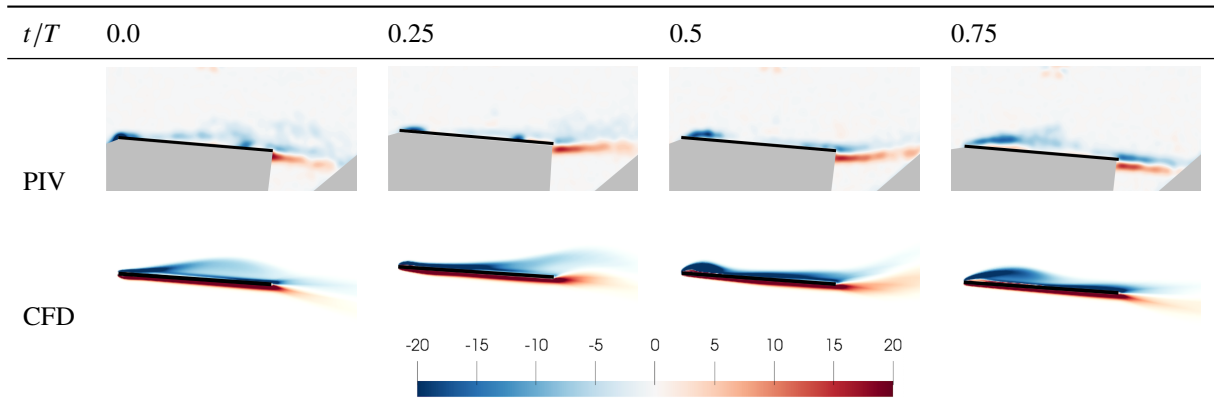


Fig. 14 Normalized spanwise vorticity $\omega_y c/U$ comparison between experimental PIV data and CFD for case 3: $k = 1$, $h_0/c = 0.05$, $\text{AR} = 3$ and $y = 0.5s$.

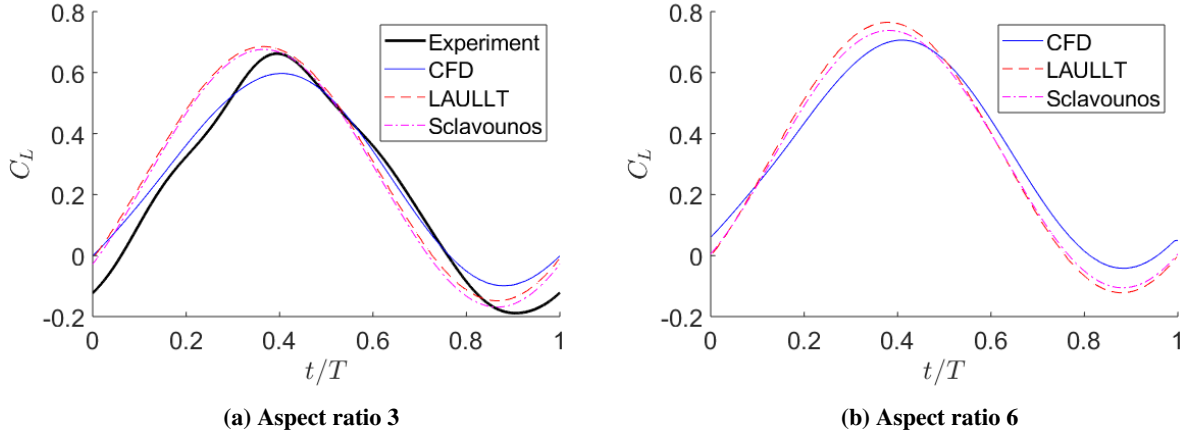


Fig. 15 C_L history for case 3: $k = 1.0, h_0/c = 0.05$

D. Case 4: $k = 1, h_0/c = 0.5$

Chord reduced frequency is set to $k = 1$ and amplitude is set to $h_0/c = 0.5$. Figure 16 and Figure 17 show the vorticity field computed by the CFD for the aspect ratio 3 and 6 wing respectively. For the AR = 3 case, a Q-criterion iso-surface is also given in Figure 18 and a comparison to PIV data shown in Figure 19.

At both aspect ratios the flow near the tip is similar in topology. At times $t/T = 0.0$ and $t/T = 0.5$, the complexity is due to the merging of vortex filaments, most easily visualized in Figure 18. This is discussed in [36, 37]. At times $t/T = 0.25$ and $t/T = 0.75$, the tip vorticity is comparatively simpler, with a cone of vorticity being formed.

At aspect ratio 3, LEVs are formed on both strokes at the quarter-span and mid-span. This is shown by both PIV data and CFD data in Figure 19. An LEV forms on the top surface on the top surface on the downwards stroke ($0.25 < t/T < 0.75$) and is shed into the trailing edge wake during the upwards stroke. The three dimensional shape of the LEV changes as it travels along the upper surface to form an arch over the centre of the wing. This is seen in Figure 18.

A smaller LEV forms on the underside of the wing during the upwards stroke ($-0.25 < t/T < 0.25$). This travels along the bottom surface of the airfoil during the downwards stroke ($0.25 < t/T < 0.75$) before being shed into the trailing edge wake. The LEV forms an arch structure on the underside during the downwards stroke.

The phenomena at aspect ratio 6 are similar, albeit stronger LEVs are formed.

Figure 20a shows the lift history for the aspect ratio 3 case. The CFD and experiment are in good agreement, in particular with respect to the non-sinusoidal shape of the C_L waveform. The LAULLT predicts a larger lift amplitude than the Sclavounos ULLT, and is in better agreement with the CFD / experiment with respect to phase.

The results for aspect ratio 6 are shown in Figure 20b. The trough of the CFD result deviates further from sinusoidal than at aspect ratio 3. At the peak, the CFD is well matched by the LAULLT, although the LAULLT trough is significantly lower. The Sclavounos / Prandtl ULLT predicts a lower lift amplitude than the LAULLT. Consequently it the peak C_L is lower than that of the CFD. The trough value is in reasonable agreement however. The LAULLT is in better phase agreement with the CFD.

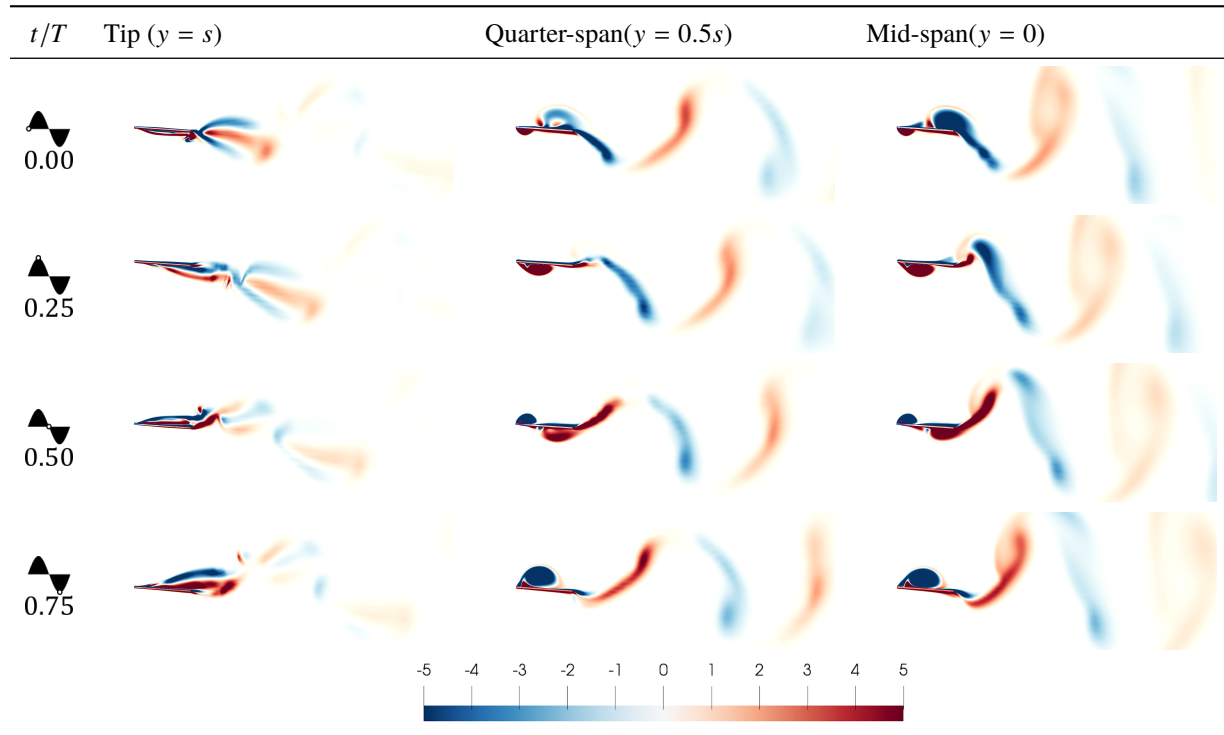


Fig. 16 Normalized spanwise vorticity $\omega_y c/U$ from CFD for case 4: $k = 1, h_0/c = 0.5, \text{AR} = 3$.

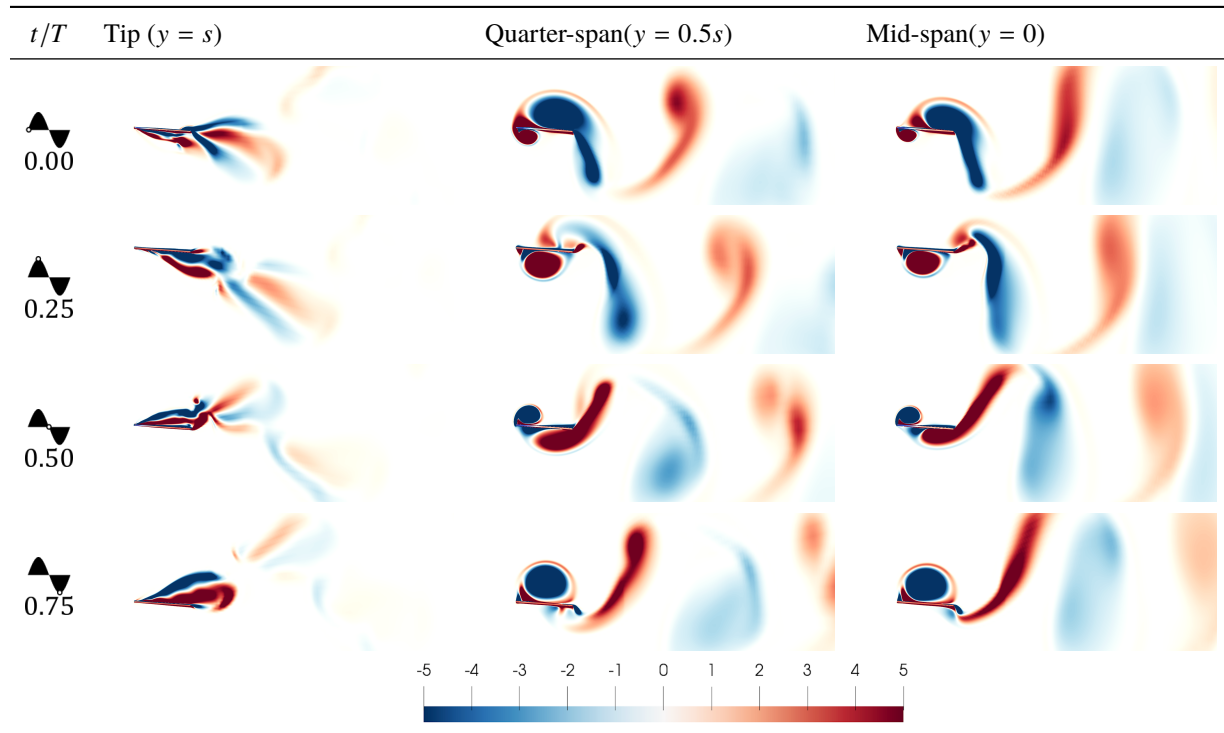


Fig. 17 Normalized spanwise vorticity $\omega_y c/U$ from CFD for case 4: $k = 1, h_0/c = 0.5, \text{AR} = 6$.

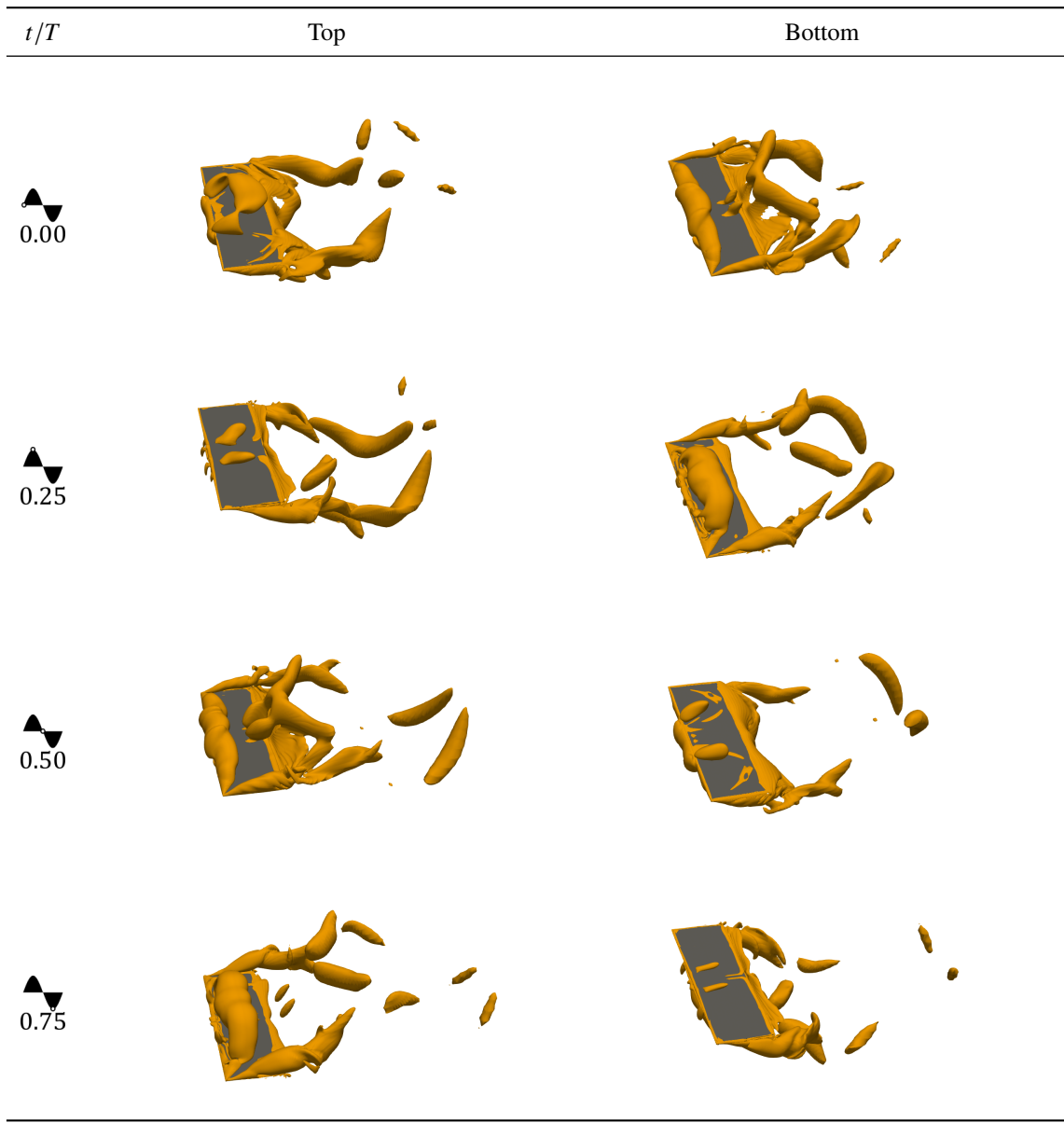


Fig. 18 Q-criterion $Q = 5$ iso-surface for case 4: $k = 1$, $h_0/c = 0.5$ AR = 3.

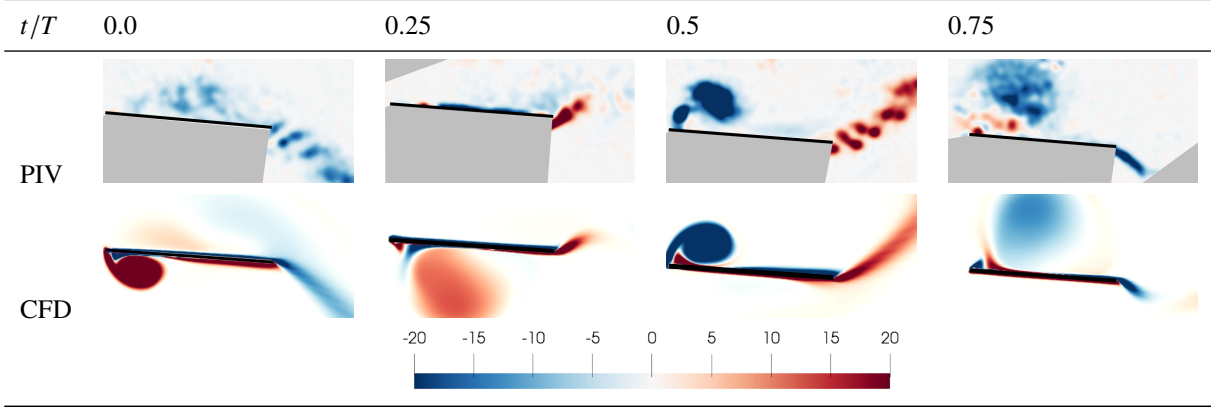


Fig. 19 Normalized spanwise vorticity $\omega_y c/U$ comparison between experimental PIV data and CFD for case 4: $k = 1$, $h_0/c = 0.5$, $\text{AR} = 3$ and $y = 0.5\text{s}$.

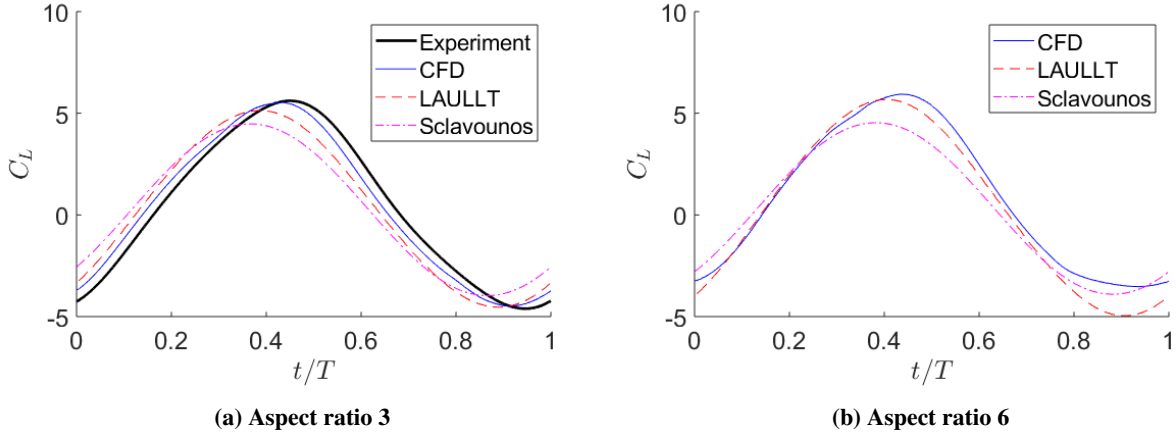


Fig. 20 C_L history for case 4: $k = 1.0$, $h_0/c = 0.5$

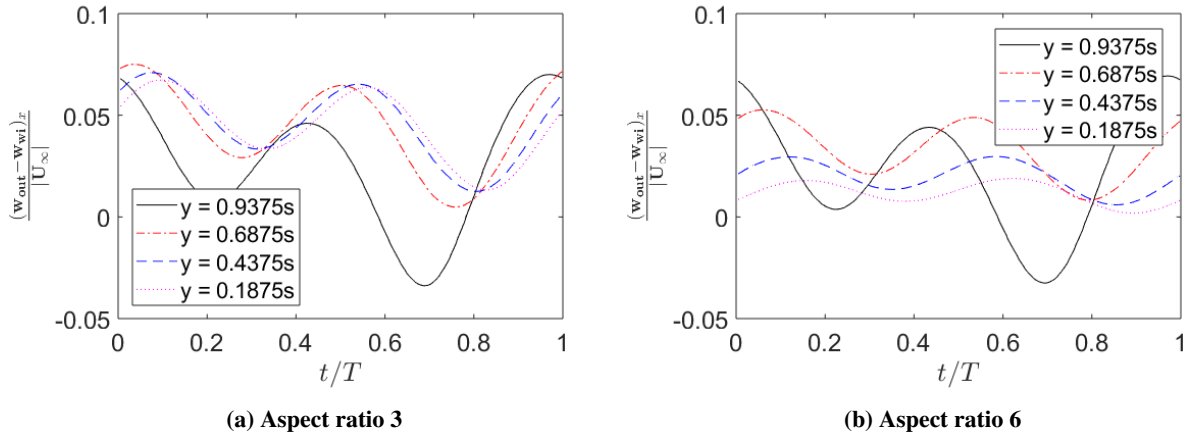


Fig. 21 The x component of the 3D induced velocity on the inner solutions at various points on the wing span in case 4.

Finally, Figure 21 shows the three dimensional effects of the LAULLT on the inner solutions at various points on the

wing. The induced velocity in the streamwise direction is shown. At both aspect ratios non-negligible velocities are induced by the LAULLT. Since the Sclavounos ULLT assumes a planar wake, it neglects these induced velocities.

VI. Conclusions

A large amplitude unsteady lifting-line theory (LAULLT) has been formulated using a large-amplitude thin airfoil theory as the inner solution. The model features a three dimensional wake in the outer solution.

The LAULLT and a frequency-domain small-amplitude ULLT were verified against experiment and computational fluid dynamics for a rectangular plate oscillating in plunge for two aspect ratios, two chord reduced frequencies and two oscillation amplitudes. It was found that both lifting-line theories were generally in agreement with experiment and CFD.

The LAULLT was generally in very close agreement with the small-amplitude ULLT, albeit usually predicting marginally higher lift amplitudes. Increasing frequency and amplitude caused it to increases lift amplitude prediction relative to the small-amplitude ULLT, and introduced a small phase lag, better matching experimental results. The lift average also changed according to frequency and amplitude.

Results from this study demonstrate that ULLT is a promising approach for low-order modelling of complex 3D unsteady aerodynamics. Efforts to model flow separation, LEV formation and LEV shedding are ongoing.

Appendix

Table 2 Amplitude and average of C_L for case 1: $h_0/c = 0.05, k = 0.4$.

Data source	Aspect ratio AR = 3		Aspect ratio AR = 6	
	C_L amplitude	C_L average	C_L amplitude	C_L average
Experiment	0.133	0.224		
CFD	0.132	0.251	0.155	0.338
LAULLT	0.127	0.268	0.146	0.321
Sclavounos / Prandtl	0.126	0.254	0.139	0.316

Table 3 Amplitude and average of C_L for case 2: $h_0/c = 0.5, k = 0.4$.

Data source	Aspect ratio AR = 3		Aspect ratio AR = 6	
	C_L amplitude	C_L average	C_L amplitude	C_L average
Experiment	1.71	0.303		
CFD	1.46	0.334	1.66	0.416
LAULLT	1.30	0.264	1.5134	0.321
Sclavounos / Prandtl	1.26	0.254	1.39	0.316

Table 4 Amplitude and average of C_L for case 3: $h_0/c = 0.05, k = 1$.

Data source	Aspect ratio AR = 3		Aspect ratio AR = 6	
	C_L amplitude	C_L average	C_L amplitude	C_L average
Experiment	0.424	0.226		
CFD	0.348	0.257	0.374	0.339
LAULLT	0.417	0.269	0.443	0.322
Sclavounos / Prandtl	0.423	0.254	0.422	0.316

Table 5 Amplitude and average of C_L for case 4: $h_0/c = 0.5$, $k = 1$.

Data source	Aspect ratio AR = 3		Aspect ratio AR = 6	
	C_L amplitude	C_L average	C_L amplitude	C_L average
Experiment	5.11	0.416		
CFD	5.01	0.645	4.73	1.20
LAULLT	4.84	0.296	5.32	0.374
Sclavounos / Prandtl	4.23	0.254	4.22	0.317

Acknowledgements

The authors gratefully acknowledge the support of the UK Engineering and Physical Sciences Research Council (EPSRC) through a DTA scholarship and grant EP/R008035.

References

- [1] Shyy, W., Lian, Y., Tang, J., Viieru, D., and Liu, H., *Aerodynamics of Low Reynolds Number Flyers*, Cambridge University Press, 2008. doi:10.1017/cbo9780511551154.
- [2] Ford, C. W. P., and Babinsky, H., “Lift and the leading-edge vortex,” *Journal of Fluid Mechanics*, Vol. 720, 2013, pp. 280–313. doi:10.1017/jfm.2013.28.
- [3] Rostami, A. B., and Armandei, M., “Renewable energy harvesting by vortex-induced motions: Review and benchmarking of technologies,” *Renewable and Sustainable Energy Reviews*, Vol. 70, 2017, pp. 193–214. doi:10.1016/j.rser.2016.11.202.
- [4] Wang, Z., Chen, P. C., Liu, D. D., and Mook, D. T., “Nonlinear-Aerodynamics/Nonlinear-Structure Interaction Methodology for a High-Altitude Long-Endurance Wing,” *Journal of Aircraft*, Vol. 47, No. 2, 2010, pp. 556–566. doi:10.2514/1.45694.
- [5] Hansen, M., Sørensen, J., Voutsinas, S., Sørensen, N., and Madsen, H., “State of the art in wind turbine aerodynamics and aeroelasticity,” *Progress in Aerospace Sciences*, Vol. 42, No. 4, 2006, pp. 285–330. doi:10.1016/j.paerosci.2006.10.002.
- [6] Liu, Y., Xie, C., Yang, C., and Cheng, J., “Gust response analysis and wind tunnel test for a high-aspect ratio wing,” *Chinese Journal of Aeronautics*, Vol. 29, No. 1, 2016, pp. 91–103. doi:10.1016/j.cja.2015.12.013, URL <https://www-sciencedirect-com.ezproxy.lib.gla.ac.uk/science/article/pii/S1000936115002423>.
- [7] Murua, J., Palacios, R., and Graham, J. M. R., “Applications of the unsteady vortex-lattice method in aircraft aeroelasticity and flight dynamics,” *Progress in Aerospace Sciences*, Vol. 55, 2012, pp. 46–72. doi:10.1016/j.paerosci.2012.06.001.
- [8] Blondeaux, P., Fornarelli, F., Guglielmini, L., Triantafyllou, M. S., and Verzicco, R., “Numerical experiments on flapping foils mimicking fish-like locomotion,” *Physics of Fluids*, Vol. 17, No. 11, 2005, p. 113601. doi:10.1063/1.2131923.
- [9] Dong, H., Mittal, R., and Najjar, F. M., “Wake topology and hydrodynamic performance of low-aspect-ratio flapping foils,” *Journal of Fluid Mechanics*, Vol. 566, 2006, p. 309. doi:10.1017/s002211200600190x.
- [10] Visbal, M., Yilmaz, T. O., and Rockwell, D., “Three-dimensional vortex formation on a heaving low-aspect-ratio wing: Computations and experiments,” *Journal of Fluids and Structures*, Vol. 38, 2013, pp. 58–76. doi:10.1016/j.jfluidstructs.2012.12.005.
- [11] Winckelmans, G., Cocle, R., Dufresne, L., and Capart, R., “Vortex methods and their application to trailing wake vortex simulations,” *Comptes Rendus Physique*, Vol. 6, No. 4-5, 2005, pp. 467–486. doi:10.1016/j.crhy.2005.05.001.
- [12] Eldredge, J., Wang, C., and OL, M., “A Computational Study of a Canonical Pitch-Up, Pitch-Down Wing Maneuver,” *39th AIAA Fluid Dynamics Conference*, American Institute of Aeronautics and Astronautics, 2009. doi:10.2514/6.2009-3687.
- [13] Katz, J., and Plotkin, A., *Low Speed Aerodynamics*, 2nd ed., Cambridge University Press, 2001.
- [14] Drela, M., “XFOIL: An Analysis and Design System for Low Reynolds Number Airfoils,” *Lecture Notes in Engineering*, Springer Berlin Heidelberg, 1989, pp. 1–12. doi:10.1007/978-3-642-84010-4_1.

- [15] Hepperle, M., *JavaFoil user's guide*, 2014.
- [16] McGowan, G. Z., Granlund, K., Ol, M. V., Gopalarathnam, A., and Edwards, J. R., “Investigations of Lift-Based Pitch-Plunge Equivalence for Airfoils at Low Reynolds Numbers,” *AIAA Journal*, Vol. 49, No. 7, 2011, pp. 1511–1524. doi:10.2514/1.j050924.
- [17] Theodorsen, T., “General Theory of Aerodynamic instability and the mechanism of flutter,” Tech. Rep. 496, NACA, 1935.
- [18] Isaacs, R., “Airfoil Theory for Flows of Variable Velocity,” *Journal of the Aeronautical Sciences*, Vol. 12, No. 1, 1945, pp. 113–117. doi:10.2514/8.11202.
- [19] Greenberg, J. M., “Airfoil in sinusoidal motion in a pulsating stream,” Tech. rep., NACA, Jun. 1947.
- [20] Wagner, H., “Über die Entstehung des dynamischen Auftriebes von Tragflügeln,” *ZAMM - Zeitschrift für Angewandte Mathematik und Mechanik*, Vol. 5, No. 1, 1925, pp. 17–35. doi:10.1002/zamm.19250050103.
- [21] Sears, W. R., “Some Aspects of Non-Stationary Airfoil Theory and Its Practical Application,” *Journal of the Aeronautical Sciences*, Vol. 8, No. 3, 1941, pp. 104–108. doi:10.2514/8.10655.
- [22] Karman, T. V., “Airfoil Theory for Non-Uniform Motion,” *Journal of the Aeronautical Sciences*, Vol. 5, No. 10, 1938, pp. 379–390. doi:10.2514/8.674.
- [23] Leishman, G. J., *Principles of Helicopter Aerodynamics*, Cambridge University Press, 2006.
- [24] Garrick, I. E., “On some reciprocal relations in the theory of nonstationary flows,” Tech. rep., NACA, 1938.
- [25] McCune, J. E., Lam, C.-M. G., and Scott, M. T., “Nonlinear aerodynamics of two-dimensional airfoils in severe maneuver,” *AIAA Journal*, Vol. 28, No. 3, 1990, pp. 385–393. doi:10.2514/3.10403.
- [26] Yan, Z., Taha, H. E., and Hajj, M. R., “Geometrically-exact unsteady model for airfoils undergoing large amplitude maneuvers,” *Aerospace Science and Technology*, Vol. 39, 2014, pp. 293–306. doi:10.1016/j.ast.2014.09.021.
- [27] Ramesh, K., Gopalarathnam, A., Edwards, J. R., Ol, M. V., and Granlund, K., “An unsteady airfoil theory applied to pitching motions validated against experiment and computation,” *Theoretical and Computational Fluid Dynamics*, Vol. 27, No. 6, 2013, pp. 843–864. doi:10.1007/s00162-012-0292-8.
- [28] McCroskey, W. J., “The Phenomenon of Dynamic Stall,” Tech. rep., NASA, Mar. 1981. URL <https://ntrs.nasa.gov/archive/nasa/casi.ntrs.nasa.gov/19810011501.pdf>.
- [29] Darakananda, D., and Eldredge, J. D., “A versatile taxonomy of low-dimensional vortex models for unsteady aerodynamics,” *Journal of Fluid Mechanics*, Vol. 858, 2018, pp. 917–948. doi:10.1017/jfm.2018.792.
- [30] Brown, C. E., and Michael, W. H., “Effect of Leading-Edge Separation on the Lift of a Delta Wing,” *Journal of the Aeronautical Sciences*, Vol. 21, No. 10, 1954, pp. 690–694. doi:10.2514/8.3180.
- [31] Michelin, S., and Smith, S. G. L., “An unsteady point vortex method for coupled fluid–solid problems,” *Theoretical and Computational Fluid Dynamics*, Vol. 23, No. 2, 2009, pp. 127–153. doi:10.1007/s00162-009-0096-7.
- [32] Ramesh, K., Gopalarathnam, A., Granlund, K., Ol, M. V., and Edwards, J. R., “Discrete-vortex method with novel shedding criterion for unsteady aerofoil flows with intermittent leading-edge vortex shedding,” *Journal of Fluid Mechanics*, Vol. 751, 2014, pp. 500–538. doi:10.1017/jfm.2014.297.
- [33] Sarpkaya, T., “An inviscid model of two-dimensional vortex shedding for transient and asymptotically steady separated flow over an inclined plate,” *Journal of Fluid Mechanics*, Vol. 68, No. 01, 1975, p. 109. doi:10.1017/s0022112075000717.
- [34] Katz, J., “A discrete vortex method for the non-steady separated flow over an airfoil,” *Journal of Fluid Mechanics*, Vol. 102, No. -1, 1981, p. 315. doi:10.1017/s0022112081002668.
- [35] Jones, M. A., “The separated flow of an inviscid fluid around a moving flat plate,” *Journal of Fluid Mechanics*, Vol. 496, 2003, pp. 405–441. doi:10.1017/s0022112003006645.
- [36] Ellenrieder, K. D. V., Parker, K., and Soria, J., “Flow structures behind a heaving and pitching finite-span wing,” *Journal of Fluid Mechanics*, Vol. 490, 2003, pp. 129–138. doi:10.1017/s0022112003005408.
- [37] Buchholz, J. H. J., and Smits, A. J., “On the evolution of the wake structure produced by a low-aspect-ratio pitching panel,” *Journal of Fluid Mechanics*, Vol. 546, No. -1, 2005, p. 433. doi:10.1017/s0022112005006865.

- [38] James, E. C., “Lifting-line theory for an unsteady wing as a singular perturbation problem,” *Journal of Fluid Mechanics*, Vol. 70, No. 04, 1975, p. 753. doi:10.1017/s0022112075002339.
- [39] Holten, T. V., “The computation of aerodynamic loads on helicopter blades in forward flight using the method of the acceleration potential,” Tech. rep., Delft University of Technology, 1975. URL <https://repository.tudelft.nl/islandora/object/uuid:4b671dde-3b0b-4a8e-9ec6-799d631ecb54?collection=research>.
- [40] Ahmadi, A. R., and Widnall, S. E., “Unsteady lifting-line theory as a singular perturbation problem,” *Journal of Fluid Mechanics*, Vol. 153, 1985, p. 59. doi:10.1017/s0022112085001148.
- [41] Sclavounos, P. D., “An unsteady lifting-line theory,” *Journal of Engineering Mathematics*, Vol. 21, No. 3, 1987, pp. 201–226. doi:10.1007/bf00127464.
- [42] Guermond, J.-L., and Sellier, A., “A unified unsteady lifting-line theory,” *Journal of Fluid Mechanics*, Vol. 229, 1991, p. 427. doi:10.1017/s0022112091003099.
- [43] Onoue, K., and Breuer, K. S., “A scaling for vortex formation on swept and unswept pitching wings,” *Journal of Fluid Mechanics*, Vol. 832, 2017, pp. 697–720. doi:10.1017/jfm.2017.710.
- [44] Lentink, D., and Dickinson, M. H., “Rotational accelerations stabilize leading edge vortices on revolving fly wings,” *Journal of Experimental Biology*, Vol. 212, No. 16, 2009, pp. 2705–2719. doi:10.1242/jeb.022269.
- [45] Yilmaz, T. O., and Rockwell, D., “Flow structure on finite-span wings due to pitch-up motion,” *Journal of Fluid Mechanics*, Vol. 691, 2011, pp. 518–545. doi:10.1017/jfm.2011.490.
- [46] Voutsinas, S. G., “Vortex methods in aeronautics: how to make things work,” *International Journal of Computational Fluid Dynamics*, Vol. 20, No. 1, 2006, pp. 3–18. doi:10.1080/10618560600566059.
- [47] Willis, D. J., Peraire, J., and White, J. K., “A combined pFFT-multipole tree code, unsteady panel method with vortex particle wakes,” *International Journal for Numerical Methods in Fluids*, Vol. 53, No. 8, 2007, pp. 1399–1422. doi:10.2514/6.2005-854.
- [48] Barnes, J., and Hut, P., “A hierarchical O(N log N) force-calculation algorithm,” *Nature*, Vol. 324, No. 6096, 1986, pp. 446–449. doi:10.1038/324446a0.
- [49] Greengard, L., and Rokhlin, V., “A Fast Algorithm for Particle Simulations,” *Journal of Computational Physics*, Vol. 135, No. 2, 1997, pp. 280–292. doi:10.1006/jcph.1997.5706.
- [50] Winckelmans, G. S., Salmon, J. K., Warren, M. S., Leonard, A., and Jodoin, B., “Application of fast parallel and sequential tree codes to computing three-dimensional flows with the vortex element and boundary element methods,” *ESAIM: Proceedings*, Vol. 1, 1996, pp. 225–240. doi:10.1051/proc:1996039.
- [51] Hirato, Y., Shen, M., Aggarwal, S., Gopalarathnam, A., and Edwards, J. R., “Initiation of Leading-Edge-Vortex Formation on Finite Wings in Unsteady Flow,” *53rd AIAA Aerospace Sciences Meeting*, American Institute of Aeronautics and Astronautics, 2015. doi:10.2514/6.2015-0546.
- [52] Devinant, P., “An approach for unsteady lifting-line time-marching numerical computation,” *International Journal for Numerical Methods in Fluids*, Vol. 26, No. 2, 1998, pp. 177–197. doi:10.1002/(sici)1097-0363(19980130)26:2<177::aid-fld633>3.3.co;2-g.
- [53] Boutet, J., and Dimitriadis, G., “Time domain analytical unsteady aerodynamic modelling for finite wings,” *55th AIAA Aerospace Sciences Meeting*, American Institute of Aeronautics and Astronautics, 2017. doi:10.2514/6.2017-0493, AIAA 2017-0493.
- [54] Ramesh, K., Monteiro, T. P., Silvestre, F. J., Bernardo, A., aes Neto, G., de Souza Siqueria Versiani, T., and da Silva, R. G. A., “Experimental and Numerical Investigation of Post-Flutter Limit Cycle Oscillations on a Cantilevered Flat Plate,” *International Forum on Aeroelasticity and Structural Dynamics 2017*, 2017. URL <http://eprints.gla.ac.uk/154722/>.
- [55] Prandtl, L., “Applications of Modern Hydrodynamics to Aeronautics,” Tech. rep., NACA, 1923. Rep. 116.
- [56] Devinant, P., and Gallois, T., “Swept and curved wings: a numerical approach based on generalized lifting-line theory,” *Computational Mechanics*, Vol. 29, No. 4-5, 2002, pp. 322–331. doi:10.1007/s00466-002-0345-8.
- [57] Vatistas, G. H., Kozel, V., and Mih, W. C., “A simpler model for concentrated vortices,” *Experiments in Fluids*, Vol. 11, No. 1, 1991, pp. 73–76. doi:10.1007/bf00198434.

- [58] Press, W. H., Teukolsky, S. A., Vetterling, W. T., and Flannery, B. P., *Numerical Recipes in C*, 2nd ed., Cambridge University Press, 1992.
- [59] Bird, H. J. A., and Ramesh, K., “Theoretical and computational studies of a rectangular finite wing oscillating in pitch and heave,” *6th European Conference on Computational Mechanics (ECCM 6) 7th European Conference on Computational Fluid Dynamics (ECFD 7)*, International Centre for Numerical Methods in Engineering, 2018.
- [60] Spalart, P., and Allmaras, S., “A one-equation turbulence model for aerodynamic flows,” *30th Aerospace Sciences Meeting and Exhibit*, American Institute of Aeronautics and Astronautics, 1992. doi:10.2514/6.1992-439, aIAA Paper 1992-0439.